J. Appl. Comput. Mech., xx(x) (2026) 1-26
DOI: 10.22055/jacm.2026.49723.6193

ISSN: 2383-4536
jacm.scu.ac.ir



Shahid Chamran
University of Ahvaz

Journal of
Applied and Computational Mechanics



Research Paper

Data-Driven and Analytical Investigation of Free Vibration in Agglomerated FG-CNT Coated Nanoshells

Mohamed S. Abd-Elwahed[1], Ahmed A. Daikh[2,3], Amin Sami Hamdi[4], Rania Gamal[5], Mohamed A. Eltaher[1]

[1] Mechanical Engineering Department, Faculty of Engineering, King Abdulaziz University, Jeddah 21589, Saudi Arabia

[2] Artificial Intelligence Laboratory for Mechanical and Civil Structures, and Soil, University Centre of Naama, P.O. Box 66, Naama 45000, Algeria

[3] Laboratoire d'Étude des Structures et de Mécanique des Matériaux, Département de Génie Civil, Faculté des Sciences et de la Technologie, Université Mustapha Stambouli B.P. 305, R.P.29000 Mascara, Algérie

[4] Department of Civil Engineering, Faculty of Engineering, King Abdulaziz University, Jeddah, Saudi Arabia

[5] Faculty of Engineering Technology Elsewedy University of Technology-Polytechnic Egypt Cairo 7060010, Egypt

Received August 23 2026; Revised September 27 2026; Accepted for publication October 13 2026.
✉ Corresponding author: M.A. Eltaher (mohaeltaher@gmail.com & meltaher@kau.edu.sa)
© 2026 Published by Shahid Chamran University of Ahvaz

Abstract. This study presents a unified analytical and data-driven framework for predicting free vibration frequencies of coated functionally graded carbon nanotube-reinforced (FG-CNT) nanoshells. This study examines two coated FG schemes (Hardcore and Softcore) combined with multiple material distribution patterns. A comprehensive analytical database is generated using higher-order shear deformation theory (HSDT) and the Galerkin method, incorporating nonlocal strain-gradient (NSGT) size effects and accounting for CNT agglomeration through a two-parameter homogenization model. The governing equations are derived via Hamilton's principle and solved analytically for shells resting on Winkler–Pasternak elastic foundations under various boundary conditions. A Random Forest regression surrogate model is trained on this analytical database, delivering exceptional prediction accuracy with computational efficiency dramatically improved relative to repeated analytical evaluation. SHAP (Shapley Additive Explanations) analysis identifies the dominant parameters governing vibration response and preserves physical interpretability. Parametric studies reveal that CNT agglomeration significantly degrades effective stiffness, while material grading indices enhance Hardcore shell rigidity but reduce Softcore shell stiffness. The proposed framework enables rapid frequency prediction for design optimization and structural health monitoring applications without repeatedly solving governing equations.

Keywords: Random Forest regression; Coated carbon nanotubes; Agglomeration; Free vibration Shells; Nonlocal strain gradient theory.

1. Introduction

Carbon nanotubes (CNTs) are cylindrical nanostructures composed of carbon atoms arranged in a highly ordered lattice, distinguished by their high aspect ratio and exceptional mechanical, electrical, and thermal properties. Since 1991, CNTs have attracted substantial research interest because of their remarkable combination of high strength, low density, and superior conductive characteristics. Their tensile strength is significantly higher than that of steel, while their excellent electrical and thermal conductivity has enabled broad applications in electronics, energy storage, materials engineering, and biomedicine. However, the high aspect ratio, low bending stiffness, and strong van der Waals interactions between CNTs promote clustering into bundles or agglomerates, which can substantially influence their effective material properties.

The continuous advancement of composites has provided materials with excellent properties and durability for modern engineering applications. While recent literature has extensively investigated conventional composite structures [1], materials science continues to enhance structural performance by developing novel advanced composites. Consequently, these advanced materials have transformed structural design, with functionally graded materials (FGMs) emerging as a particularly important class of engineered composites. Unlike conventional composites with sharp interfaces between constituent materials, FGMs exhibit a continuous variation in composition and properties, commonly transitioning between metallic and ceramic phases. This gradual variation provides enhanced adaptability to complex mechanical, thermal, and vibrational environments [2]. As a result, FGMs offer improved resistance to thermal stresses, reduced stress concentrations, and optimized stiffness-to-weight performance, making them highly attractive for demanding applications in aerospace, nuclear, and biomedical engineering [3, 4].

A growing body of research has examined the influence of carbon nanotube agglomeration on the mechanical and vibrational behavior of carbon nanotube-reinforced composites (CNTRCs) [5]. Shi et al. [6] developed a two-parameter agglomeration model to estimate the effective properties of CNTRCs, accounting for the effects of nanotube waviness and agglomeration in composites

Published online: November 20 2026

reinforced with randomly oriented straight CNTs. Hedayati and Sobhani Aragh [7] further investigated the effect of graded CNT agglomeration on the free vibration behavior of annular sector plates resting on a Pasternak foundation, while Heshmati and Yas [8] showed that CNT agglomeration has a significant weakening effect on the dynamic behavior of functionally graded nanocomposite beams.

Subsequent studies extended this line of work to a wide range of structural configurations. Aragh et al. [9] examined the natural frequencies of CNT-reinforced cylindrical shells, whereas Kamarian et al. [10, 11] investigated the effects of CNT agglomeration on the free vibration behavior of functionally graded CNTRC Timoshenko beams and conical shells, respectively. Tornabene et al. [12, 13] also contributed substantially by analyzing the influence of agglomerated CNTs on the natural frequencies, as well as the static response, of functionally graded nanocomposite plates and shells.

Related investigations have also addressed multiscale interactions and advanced modeling approaches. Shokrieh et al. [14] emphasized the importance of the CNT–matrix interphase in micromechanical modeling and proposed the use of van der Waals forces (weak intermolecular forces between adjacent nanostructures) to represent this region and predict nanocomposite properties more accurately. Similarly, He et al. [15] and Strozzi and Mellicano [16] explored the role of van der Waals interactions in the vibration behavior of multi-walled and triple-walled CNT systems. In addition, Barai and Weng [17] developed a two-scale micromechanical model to examine the combined effects of interface behavior and CNT agglomeration on the plastic strength of composites. Yusufoglu and Avey [18] developed an analytical solution of the nonlinear dynamic behavior of CNT-based hyperbolic paraboloidal shallow shells with various distribution shapes.

More recent studies have expanded the scope to increasingly sophisticated composite systems. Nejati et al. [19] employed the generalized differential quadrature method to perform static and free vibration analyses of agglomerated functionally graded conical shells, while Bisheh et al. [20] proposed an analytical model for wave propagation in piezoelectric composite cylindrical shells reinforced with agglomerated CNTs. Zhang et al. [21] used the element-free IMLS-Ritz method combined with first-order shear deformation theory to study the effects of geometric and material parameters on plate vibration. Ziaei et al. [22] investigated the effect of CNT agglomerates on residual stresses in fiber-reinforced nanocomposites using both experimental and analytical approaches. More recently, Tavakoli et al. [23] applied the generalized differential quadrature method to analyze the free vibration of three-phase agglomerated fiber/CNT/polymer nanocomposite conical shells. Ajri [24] examined the nonlinear post-buckling behavior of FG cylindrical copper shell reinforced with CNTs with a polymer core. Ozalp and Esen [25] studied the thermal stability of a doubly-curved sandwich nanoplate with symmetric functionally graded face layers. Nguyen et al. [26] studied the free vibration analysis of rotating stiffened advanced nanocomposite toroidal shell segments in thermal environments. Saidi et al. [27] presented a theoretical framework to analyze the dynamic thermoelastic response of a solid cylinder containing microscopic voids under a sudden thermal shock at its lateral surface.

Many researchers have recently considered the applicability of machine learning and deep learning to analysing structural vibration responses. Avci et al. [28] reviewed vibration-based damage detection in civil structures, from traditional methods to machine learning and deep learning applications. Jakkamputi et al. [29] diagnosed and detected defects in the vibration of high-performance composite structures using a machine learning approach. Challagulla et al. [30] evaluated damping modification factors for floor response spectra by using a machine learning model. de Sousa et al. [31] concluded that structural monitoring using a machine learning algorithm achieved excellent metrics when using a simulation-generated dataset. Yan et al. [32] developed a simplified approach to recognize vortex-induced vibration response using machine learning. Lin and Ibraheem [33] used machine learning to estimate vibrations in concrete structures reinforced with advanced nanocomposites. Zheng et al. [34] used machine learning and numerical approaches for vibration behavior prediction of rotating nanobeams in complex environments.

At the nanoscale, classical continuum mechanics fails to capture size-dependent phenomena, necessitating advanced size-dependent continuum theories. Over the past decades, researchers have developed various higher-order theories to address this limitation. For instance, classical Nonlocal Elasticity Theory (NET) is widely used to capture the stiffness-softening effect caused by long-range interatomic interactions [35]. Conversely, the Modified Couple Stress Theory (MCST) [36] and Strain Gradient Theory (SGT) [37] introduce material length-scale parameters that account for the stiffness-hardening effects observed in micro/nanostructures. Additionally, Surface Elasticity Theory [38, 39] is often used to capture the strong influence of surface energy and residual surface stresses that arise from the high surface-area-to-volume ratio of nanomaterials.

However, NET, MCST, and surface elasticity typically capture only one specific scale effect in isolation (softening, hardening, or surface traction). Recently, modified nonlocal strain gradient theories have been proposed to further refine higher-order constitutive relations and non-classical boundary conditions in complex nanostructures [40-42]. Building upon these theoretical advancements, recent studies have extensively applied such size-dependent frameworks to investigate the multi-physical and dynamic behaviors of complex structural systems. These applications include nanoplates on viscoelastic foundations [43], the vibration-absorption capabilities of sandwich nanoshells under random loading [44], and doubly curved nanoshells integrating flexoelectric and piezoelectric effects [45, 46].

Therefore, this study examines the free vibration of agglomerated coated FG-CNT cylindrical nanoshells by considering various geometrical and material parameters. Based on previous work, machine-learning prediction of the vibration response of multi-directional functionally graded cylindrical nanoshells has not been considered elsewhere, and this article aims to fill this gap. The novelty of the present work is three-fold: first, a unified analytical framework integrating multi-directional coated FG-CNT architectures with agglomeration effects and nonlocal strain-gradient size effects in a single shell vibration formulation; second, an exact Galerkin solution providing a comprehensive analytical database for validation of surrogate models; and third, a Random Forest model with SHAP analysis that enables rapid frequency prediction while maintaining explicit traceability to the governing equations for real-time design optimization. The rest of the article is organized as follows: the material gradations and their properties are discussed in Section 2. Section 3 presents the displacement field based on higher-order shear deformation theory (HSDT). Section 4 derives the governing equations. Section 5 develops the analytical solution using the Galerkin procedure. Section 6 presents the results and discussion, including parametric studies and validation. Section 7 presents the machine learning model and its numerical predictions, including Random Forest regression and SHAP analysis.

2. Material Distribution and Graduation

The object of study is a composite shell with arbitrary principal curvatures (see Fig. 1). The shell's midplane is characterized by two principal radii of curvature, R_x and R_y, corresponding to the $x$and $y$directions, respectively. Four shell geometries are examined: (i) a spherical shell with equal principal curvatures, (ii) a cylindrical shell with curvature in one principal direction, (iii) a hyperbolic-paraboloidal shell with opposite principal curvatures, and (iv) an elliptical-paraboloidal shell with unequal positive principal curvatures.



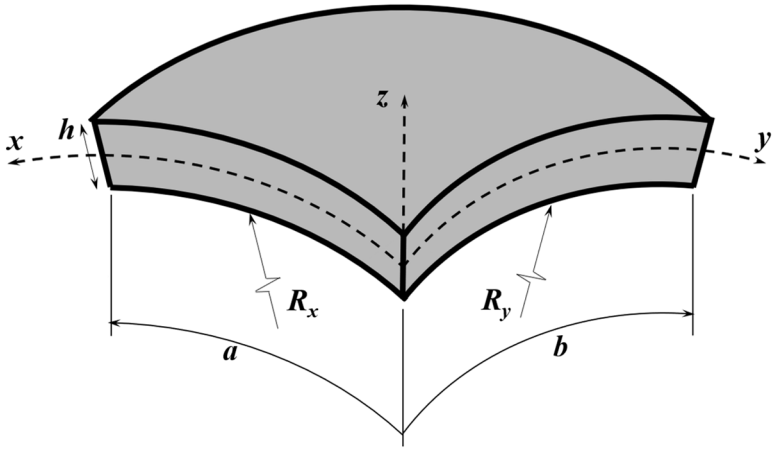


Fig. 1. Tri-coated FG spherical shell geometry.

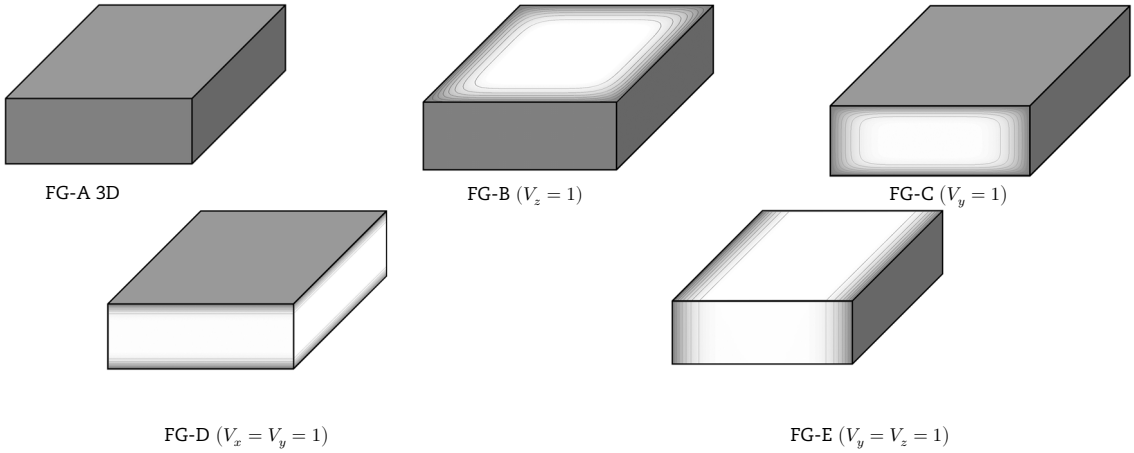


Fig. 2. Various schemes of coated FG shell $(R_x = R_y = \infty)$.

The parameters a and b denote the arc lengths measured along the curvilinear coordinates x and y on the shell's mid-surface, representing the actual lengths of the curved paths. The shell thickness is denoted by h. This structure is constructed from an epoxy matrix reinforced with randomly distributed carbon nanotubes, with the volume fraction of CNTs varying in the three directions of the nanoshell. Two types of FG CNTs shells are analysed, namely hardcore FG shells and softcore FG shells. Five different patterns of CNT distribution are considered, including a tridirectional material distribution pattern «FG-A», two bidirectional material distribution patterns, «FG-B» and «FG-C», a unidirectional transverse material distribution «FG-D», and a unidirectional axial material distribution «FG-E» (Fig. 2).

The law of mixture can be used to calculate Young's modulus (E), mass density (ρ), and Poisson's ratio (υ) of a composite material. This law asserts that the overall properties of the composite material are determined by the properties of its individual components and their volume fractions as:

$$P(x,y,z) = P_m + (P_{cnt} - P_m)V(x,y,z) \tag{1}$$

The equation mentioned above involves two terms: P_m and P_{cnt}. Here, P_m refers to the mechanical properties of the matrix, while P_{cnt} represents the effective material properties of the CNTs constituents. The volume fraction is determined by three functions, one in each direction [47]:

$$\begin{cases} V(x) = \left[\left(\dfrac{|2x-a|}{a}\right)^k - 1\right] \\ V(y) = \left[\left(\dfrac{|2y-b|}{b}\right)^e - 1\right] \\ V(z) = \left[\left(\dfrac{|2z|}{h}\right)^p - 1\right] \end{cases} \tag{2}$$

The parameters p, k, and e are material inhomogeneity indices that govern the spatial gradation profile of the carbon nanotubes along the thickness (z-axis), longitudinal (x-axis), and transverse (y-axis) directions of the nanoshell, respectively.

The total volume fraction of the Hardcore (HC) coated FG-CNTs shell can be defined as:

$$V(x,y,z) = V(x)V(y)V(z) \tag{3}$$

and for the Softcore (SC) coated FG-CNTs shell:

$$V(x,y,z) = 1 - V(x)V(y)V(z) \tag{4}$$

Table 1. Hill's elastic moduli for (10, 10) single-walled carbon nanotubes [48].

k_{cnt} [GPa]	l_{cnt}[GPa]	m_{cnt}[GPa]	n_{cnt}[GPa]	p_{cnt}[GPa]
271	88	17	1089	442

2.1. Nanoshells reinforced by randomly oriented CNTs

For a nanocomposite material where the CNTs are randomly oriented within the polymer phase, the effective material properties can be expressed using the above equation, which assumes the composite to be isotropic:

$$E = \frac{9KG}{3K+G} \tag{5}$$

$$\nu = \frac{3K-2G}{6K+2G} \tag{6}$$

The effective bulk modulus (K) and shear modulus (G) of the CNT/polymer composite can be determined using the following equations:

$$K = K_m + \frac{V_{cnt}(\delta_{cnt} - 3K_m\alpha_{cnt})}{3(V_m + V_{cnt}\alpha_{cnt})} \tag{7}$$

$$G = G_m + \frac{V_{cnt}(\eta_{cnt} - 2G_m\beta_{cnt})}{2(V_m + V_{cnt}\beta_{cnt})} \tag{8}$$

The volume fractions of polymer and CNTs are denoted by V_m and V_{cnt}, respectively, and they are related as follows:

$$V_m = 1 - V_{cnt} \tag{9}$$

The remaining parameters in the above equations can be expressed as follows:

$$\alpha_{cnt} = \frac{3(K_m + G_m) + k_{cnt} - l_{cnt}}{3(G_m + k_{cnt})} \tag{10}$$

$$\beta_{cnt} = \frac{1}{5}\left(\frac{4G_m + 2k_{cnt} + l_{cnt}}{3(G_m + k_{cnt})} + \frac{4G_m}{G_m + p_{cnt}} + \frac{2\left(G_p(3K_m + G_m) + G_m(3K_m + 7G_m)\right)}{G_p(3K_m + G_m) + m_{cnt}(3K_m + 7G_m)}\right) \tag{11}$$

$$\delta_{cnt} = \frac{1}{3}\left(n_{cnt} + 2l_{cnt} + \frac{2(k_{cnt} + l_{cnt})(3K_m + 2G_m - l_{cnt})}{G_m + k_{cnt}}\right) \tag{12}$$

$$\eta_{cnt} = \frac{1}{5}\left(\frac{2}{3}(n_{cnt} - l_{cnt}) + \frac{8G_m p_{cnt}}{G_m + p_{cnt}} + \frac{8m_{cnt}G_m(3K_m + 4G_m)}{3K_m(m_{cnt} + G_m) + G_p(7m_{cnt} + G_m)} + \frac{2(k_{cnt} - l_{cnt})(2G_m + l_{cnt})}{3(G_m + k_{cnt})}\right) \tag{13}$$

In the context of the given statement, Table 1 lists the values of Hill's elastic moduli for (10, 10) Single-Walled Carbon Nanotubes (SWCNTs) with various chiral indices.

2.2. Nanoshells reinforced by agglomerated CNTs

In nanocomposite structures, CNT clustering and bundling lead to significant agglomeration. Therefore, the effective properties of a nanocomposite reinforced with randomly oriented CNTs, accounting for the impact of agglomeration (Fig. 3), can be determined using a two-parameter homogenization method proposed by Shi et al. [6]. According to this micromechanical model, the total volume fraction of CNTs within the selected representative volume element (RVE) is divided into two distinct parts, as shown below:

$$V_{cnt} = V_{cnt}^{\text{in-cluster}} + V_{cnt}^{\text{out-cluster}} \tag{14}$$

The terms $V_{cnt}^{\text{in-cluster}}$ and $V_{cnt}^{\text{out-cluster}}$ refer to the volume fractions of CNTs inside and outside of clusters, respectively. To incorporate the agglomeration effect, two parameters are defined as follows:

$$\begin{aligned} \zeta &= \frac{V_{\text{cluster}}}{V} \\ \xi &= \frac{V_{cnt}^{\text{in-cluster}}}{V_{cnt}} \end{aligned} \tag{15}$$

The term V_{cluster} represents the volume fraction of clusters within the assumed RVE. The CNTs agglomeration is defined by two parameters, ζ and ξ. A value of ζ close to 1 indicates a completely uniform distribution of CNT nanofillers, while a decrease in ζ indicates greater agglomeration. A value of ξ close to 1 indicates that all CNTs are located inside the clusters. When ξ is equal to ζ, it suggests no agglomeration within the nanocomposite shell.

Hill's elastic moduli are used to calculate both the effective bulk moduli and effective shear moduli of the composite material within the inclusions (K_{in} and G_{in}, respectively) and outside the inclusions (K_{out} and G_{out}, respectively):

$$K_{\text{in}} = K_m + \frac{V_{cnt}\zeta(\delta_{cnt} - 3K_m\alpha_{cnt})}{3(\xi - \zeta V_{cnt} + \zeta V_{cnt}\alpha_{cnt})} \tag{16}$$

$$K_{\text{out}} = K_m + \frac{V_{cnt}(1-\zeta)(\delta_{cnt} - 3K_m\alpha_{cnt})}{3(1 - \xi - (1-\zeta)V_{cnt} + (1-\zeta)V_{cnt}\alpha_{cnt})} \tag{17}$$

$$G_{\text{in}} = G_m + \frac{V_{cnt}\zeta(\eta_{cnt} - 2G_m\beta_{cnt})}{2(\xi - \zeta V_{cnt} + \zeta V_{cnt}\beta_{cnt})} \tag{18}$$

$$G_{\text{out}} = G_m + \frac{V_{cnt}(1-\zeta)(\eta_{cnt} - 2G_m\beta_{cnt})}{2(1-\xi-(1-\zeta)V_{cnt} + (1-\zeta)V_{cnt}\beta_{cnt})} \tag{19}$$

The effective bulk modulus and shear modulus of the CNT/polymer composite can be determined using the following equations:

$$K = K_{\text{out}}\left(1 + \frac{\xi\left(\frac{K_{\text{in}}}{K_{\text{out}}} - 1\right)}{1 + \tilde{\alpha}(1-\xi)\left(\frac{K_{\text{in}}}{K_{\text{out}}} - 1\right)}\right) \tag{20}$$

$$G = G_{\text{out}}\left(1 + \frac{\xi\left(\frac{G_{\text{in}}}{K_{\text{out}}} - 1\right)}{1 + \tilde{\beta}(1-\xi)\left(\frac{G_{\text{in}}}{G_{\text{out}}} - 1\right)}\right) \tag{21}$$

with,

$$\begin{aligned} \tilde{\alpha} &= \frac{1+\nu_{\text{out}}}{3(1-\nu_{\text{out}})} \\ \tilde{\beta} &= \frac{2(4-5\nu_{\text{out}})}{15(1-\nu_{\text{out}})} \end{aligned} \tag{22}$$

3. Displacement Field

The governing equations for the dynamic response of coated FG GRC shells are derived using a shear deformation theory based on an inverse trigonometric function. The displacement field is defined as follows [1]:

$$\begin{aligned} u(x,y,z,t) &= \left(1 + \frac{z}{R_x}\right)u_0 - z\frac{\partial w_0}{\partial x} + f(z)\psi_x \\ v(x,y,z,t) &= \left(1 + \frac{z}{R_y}\right)v_0 - z\frac{\partial w_0}{\partial y} + f(z)\psi_y \\ w(x,y,z,t) &= w_0 \end{aligned} \tag{23}$$

The composite shell's midplane displacements are u_0, v_0, and w_0, and the transverse normal rotations at $z = 0$ are denoted by ψ_x and ψ_y. In this study, a higher-order shear deformation theory is employed to overcome the inherent limitations of both classical and first-order theories. Classical plate theory (CPT) applies only to thin structures because it neglects transverse shear deformations. Conversely, first-order shear deformation theory (FSDT) accounts for these deformations but relies on an artificial shear correction factor, which limits its accuracy for complex, moderately thick structures. By adopting an HSDT framework, the non-linear distribution of transverse shear strains across the shell thickness is accurately captured, naturally satisfying the zero-traction boundary conditions at the surfaces without the need for arbitrary shear correction factors. To govern this kinematic behavior, the present study proposes the following transverse shear shape function, $f(z)$:

$$f(z) = 5h\,\text{atan}\left(\frac{z}{h}\right) - 4z \tag{24}$$

Physically, this proposed function dictates the non-linear profile of the transverse shear strains throughout the shell thickness. Its specific mathematical formulation ensures that the transverse shear stresses naturally vanish at both the upper and lower surfaces ($z = \pm h/2$), rigorously enforcing the stress-free boundary conditions.

The strains can be obtained by differentiating the displacement equation given above:

$$\begin{aligned} \begin{Bmatrix} \varepsilon_{xx} \\ \varepsilon_{yy} \\ \gamma_{xy} \end{Bmatrix} &= \begin{Bmatrix} \varepsilon^0_{xx} \\ \varepsilon^0_{yy} \\ \gamma^0_{xy} \end{Bmatrix} + z\begin{Bmatrix} \varepsilon^1_{xx} \\ \varepsilon^1_{yy} \\ \gamma^1_{xy} \end{Bmatrix} + f(z)\begin{Bmatrix} \varepsilon^2_{xx} \\ \varepsilon^2_{yy} \\ \gamma^2_{xy} \end{Bmatrix} \\ \varepsilon_{zz} = 0, \qquad \begin{Bmatrix} \gamma_{yz} \\ \gamma_{xz} \end{Bmatrix} &= \frac{\mathrm{d}f(z)}{\mathrm{d}z}\begin{Bmatrix} \gamma^0_{yz} \\ \gamma^0_{xz} \end{Bmatrix}, \end{aligned} \tag{25}$$

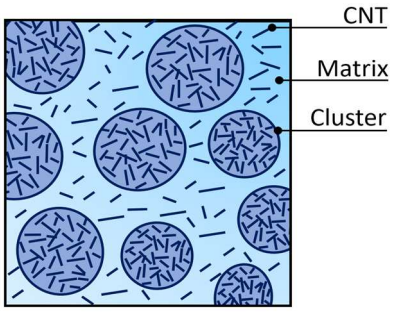


Fig. 3. Agglomeration of CNTs within the representative volume element (RVE).

where,

$$\begin{Bmatrix}\varepsilon^0_{xx}\\ \varepsilon^0_{yy}\\ \gamma^0_{xy}\end{Bmatrix}=\begin{Bmatrix}\dfrac{\partial u_0}{\partial x}+\dfrac{w_0}{R_x}\\ \dfrac{\partial v_0}{\partial y}+\dfrac{w_0}{R_y}\\ \dfrac{\partial v_0}{\partial x}+\dfrac{\partial u_0}{\partial y}\end{Bmatrix},\qquad \begin{Bmatrix}\varepsilon^1_{xx}\\ \varepsilon^1_{yy}\\ \gamma^1_{xy}\end{Bmatrix}=-\begin{Bmatrix}\dfrac{\partial^2 w_0}{\partial x^2}\\ \dfrac{\partial^2 w_0}{\partial y^2}\\ 2\dfrac{\partial^2 w_0}{\partial x\partial y}\end{Bmatrix},$$
$$\begin{Bmatrix}\varepsilon^2_{xx}\\ \varepsilon^2_{yy}\\ \gamma^2_{xy}\end{Bmatrix}=\begin{Bmatrix}\dfrac{\partial \varphi_1}{\partial x}\\ \dfrac{\partial \varphi_2}{\partial y}\\ \dfrac{\partial \varphi_2}{\partial x}+\dfrac{\partial \varphi_1}{\partial y}\end{Bmatrix},\qquad \begin{Bmatrix}\gamma^0_{yz}\\ \gamma^0_{xz}\end{Bmatrix}=\begin{Bmatrix}\varphi_x\\ \varphi_y\end{Bmatrix}. \tag{26}$$

Considering the effects of both strain gradient stress and nonlocal elastic stress, the constitutive equation for the nanoshell can be expressed as shown in [49, 4]:

$$\sigma_{ij}=\sigma^{(0)}_{ij}-\frac{d\sigma^{(1)}_{ij}}{dx} \tag{27}$$

The stress $\sigma^{(0)}_{ij}$ and the higher-order stress $\sigma^{(1)}_{ij}$ are dependent on the strain ε_{kl} and the first-order strain gradient $\varepsilon_{kl,x}$, and they can be written as [50]:

$$\sigma^{(0)}_{ij}=\int_0^L C_{ijkl}\alpha_0(x,x',e_0a)\varepsilon_{kl}(x')\mathrm{d}x' \tag{28}$$

$$\sigma^{(1)}_{ij}=l^2\int_0^L C_{ijkl}\alpha_1(x,x',e_1a)\varepsilon_{kl,x}(x')\mathrm{d}x' \tag{29}$$

where C_{ijkl} are elastic constants, l represents the material length-scale parameter that distinguishes the strain-gradient stress field. The nonlocal parameters that distinguish the field of the nonlocal elastic stress are e_0a and e_1a, and $\alpha_0(x,x',e_0a)$ and $\alpha_1(x,x',e_1a)$ are the nonlocal kernel functions. The constitutive relation is given as:

$$[1-(e_1a)^2\nabla^2][1-(e_0a)^2\nabla^2]\sigma_{ij}=C_{ijkl}[1-(e_1a)^2\nabla^2]\varepsilon_{kl}-C_{ijkl}l^2[1-(e_0a)^2\nabla^2]\nabla^2\varepsilon_{kl} \tag{30}$$

where $\nabla^2=\frac{\partial^2}{\partial x^2}+\frac{\partial^2}{\partial y^2}$ describes the Laplacian operator. The nonlocal strain gradient constitutive relations given in Eq. (12) by assuming that $e=e_0=e_1$ can be stated as [4]:

$$[1-\mu\nabla^2]\sigma_{ij}=C_{ijkl}[1-\lambda\nabla^2]\varepsilon_{kl} \tag{31}$$

where $\mu=(ea)^2$ and $\lambda=l^2$. The stress-strain relations for the nonlocal strain gradient constitutive theory are governed by:

$$\begin{Bmatrix}\sigma_{xx}-\mu\nabla^2\sigma_{xx}\\ \sigma_{yy}-\mu\nabla^2\sigma_{yy}\\ \tau_{yz}-\mu\nabla^2\tau_{yz}\\ \tau_{xz}-\mu\nabla^2\tau_{xz}\\ \tau_{xy}-\mu\nabla^2\tau_{xy}\end{Bmatrix}=\begin{bmatrix}Q_{11}&Q_{12}&0&0&0\\ Q_{12}&Q_{22}&0&0&0\\ 0&0&Q_{44}&0&0\\ 0&0&0&Q_{55}&0\\ 0&0&0&0&Q_{66}\end{bmatrix}\begin{Bmatrix}\varepsilon_{xx}-\lambda\nabla^2\varepsilon_{xx}\\ \varepsilon_{yy}-\lambda\nabla^2\varepsilon_{yy}\\ \gamma_{yz}-\lambda\nabla^2\gamma_{yz}\\ \gamma_{xz}-\lambda\nabla^2\gamma_{xz}\\ \gamma_{xy}-\lambda\nabla^2\gamma_{xy}\end{Bmatrix} \tag{32}$$

where,

$$Q_{11}=\frac{E}{1-\nu^2}\ ,\qquad Q_{22}=Q_{11},\qquad Q_{12}=\frac{\nu E}{1-\nu^2},\qquad Q_{44}=Q_{55}=Q_{66}=\frac{E}{2(1+\nu)} \tag{33}$$

Here ∇^2 describes the Laplacian operator $\left(\nabla^2=\frac{\partial^2}{\partial x^2}+\frac{\partial^2}{\partial y^2}\right)$. Integrating Eq. (32) yields the stress relations, moment, and additional moment resultants, as follows:

$$\begin{Bmatrix}\{N\}\\ \{M\}\\ \{P\}\end{Bmatrix}=\begin{bmatrix}[A]&[B]&[C]\\ [B]&[D]&[F]\\ [C]&[F]&[H]\end{bmatrix}\begin{Bmatrix}\{\varepsilon^0\}\\ \{\varepsilon^1\}\\ \{\varepsilon^2\}\end{Bmatrix} \tag{34}$$

$$\begin{Bmatrix}R_{yz}\\ R_{xz}\end{Bmatrix}=\begin{bmatrix}J_{44}&J_{45}\\ J_{45}&J_{55}\end{bmatrix}\begin{Bmatrix}\gamma^0_{yz}\\ \gamma^0_{xz}\end{Bmatrix} \tag{35}$$

where,

$$\begin{gathered}\{N\}=\{N_{xx}\quad N_{yy}\quad N_{xy}\}^T,\qquad \{M\}=\{M_{xx}\quad M_{yy}\quad M_{xy}\}^T,\qquad \{P\}=\{P_{xx}\quad P_{yy}\quad P_{xy}\}^T\\ \{\varepsilon^0\}=\{\varepsilon^0_{xx}\quad \varepsilon^0_{yy}\quad \gamma^0_{xy}\}^T,\qquad \{\varepsilon^1\}=\{\varepsilon^1_{xx}\quad \varepsilon^1_{yy}\quad \gamma^1_{xy}\}^T,\qquad \{\varepsilon^2\}=\{\varepsilon^2_{xx}\quad \varepsilon^2_{yy}\quad \gamma^2_{xy}\}^T\end{gathered} \tag{36}$$

and,

$$\begin{gathered}\{A_{ij},B_{ij},D_{ij},C_{ij},F_{ij},H_{ij}\}=\int_V Q_{ij}\{1,z,z^2,f(z),zf(z),f(z)^2\}\mathrm{d}z\,,\qquad (i,j=1,2,6)\\ J_{ii}=\int_V Q_{ii}\left[\frac{\mathrm{d}f(z)}{\mathrm{d}z}\right]^2\mathrm{d}z\ (i=4,5)\end{gathered} \tag{37}$$

4. Governing Equations

The equations of motion for the coated FG CNTs nanoshell are derived using Hamilton's principle:

$$\delta \int_{t_2}^{t_1} \delta(U - T + F)dt \;=\; 0 \tag{38}$$

The strain energy of the coated FG CNT shell can be computed as:

$$\delta U = \frac{1}{2}\int_V \left[\sigma_{xx}^{(k)}\delta\varepsilon_{xx} + \sigma_{yy}^{(k)}\delta\varepsilon_{xx} + \sigma_{xy}^{(k)}\delta\gamma_{xy} + \sigma_{xz}^{(k)}\delta\gamma_{xz} + \sigma_{yz}^{(k)}\delta\gamma_{yz}\right] dV \tag{39}$$

The kinetic energy of the coated FG CNT shell at any given moment can be formulated as:

$$\delta T = \frac{1}{2}\int_V \rho(\dot{u}\delta\dot{u} + \dot{v}\delta\dot{v} + \dot{w}\delta\dot{w})\, dV \tag{40}$$

$$\begin{aligned}\delta T = \int_V \Big\{ & I_0(\dot{u}_0\delta\dot{u}_0 + \dot{v}_0\delta\dot{v}_0 + \dot{w}_0\delta\dot{w}_0) + I_1\left(\frac{\partial\dot{w}_0}{\partial x}\delta\dot{u}_0 + \frac{\partial\dot{w}_0}{\partial y}\delta\dot{v}_0 + \dot{u}_0\frac{\partial\delta\dot{w}_0}{\partial x} + \dot{v}_0\frac{\partial\delta\dot{w}_0}{\partial y}\right) + I_2\left(\frac{\partial\dot{w}_0}{\partial x}\frac{\partial\delta\dot{w}_0}{\partial x} + \frac{\partial\dot{w}_0}{\partial y}\frac{\partial\delta\dot{w}_0}{\partial y}\right) \\ & + I_3(\dot{\varphi}_x\delta\dot{u}_0 + \dot{u}_0\delta\dot{\varphi}_x + \dot{\varphi}_y\delta\dot{v}_0 + \dot{v}_0\delta\dot{\varphi}_y) + I_4\left(\dot{\varphi}_x\frac{\partial\delta\dot{w}_0}{\partial x} + \frac{\partial\dot{w}_0}{\partial x}\delta\dot{\varphi}_x + \dot{\varphi}_y\frac{\partial\delta\dot{w}_0}{\partial y} + \frac{\partial\dot{w}_0}{\partial y}\delta\dot{\varphi}_y\right) \\ & + I_5(\dot{\varphi}_x\delta\dot{\varphi}_x + \dot{\varphi}_y\delta\dot{\varphi}_y)\Big\}\,\mathrm{d}x\mathrm{d}y\mathrm{d}z\end{aligned} \tag{41}$$

where,

$$\{I_0, I_1, I_2, I_3, I_4, I_5\} = \int_V \rho\left\{1, z, z^2, f(z), zf(z), (f(z))^2\right\} dV \tag{42}$$

The Winkler–Pasternak elastic foundation contributes an additional transverse restoring force per unit area of the form:

$$\delta F = -K_{\mathrm{w}}w(x,y) + K_{\mathrm{s}}\left(\frac{\partial^2 w(x,y)}{\partial x^2} + \frac{\partial^2 w(x,y)}{\partial y^2}\right) \tag{43}$$

where K_w is the Winkler (normal) stiffness parameter and K_s is the Pasternak (shear) stiffness parameter. Substituting Eqs. (39) and (41) into Eq. (38) yields the equilibrium equations for the coated FG CNTs nanoshell, as follows:

$$\begin{aligned}[1-\lambda\nabla^2]\Big[& A_{11}\frac{\partial^2 u_0}{\partial x^2} + A_{66}\frac{\partial^2 u_0}{\partial y^2} + (A_{12}+A_{66})\frac{\partial^2 v_0}{\partial x\partial y} + \left(\frac{A_{11}}{R_x} + \frac{A_{12}}{R_y}\right)\frac{\partial w_0}{\partial x} - B_{11}\frac{\partial^3 w_0}{\partial x^3} - (B_{12}+2B_{66})\frac{\partial^3 w_0}{\partial x\partial y^2} + B_{11}^s\frac{\partial^2\psi_x}{\partial x^2} + B_{66}^s\frac{\partial^2\psi_x}{\partial y^2} \\ & + (B_{12}^s + B_{66}^s)\frac{\partial^2\psi_y}{\partial x\partial y}\Big] = [1-\mu\nabla^2]\left[\left(I_0 + 2\frac{I_1}{R_x} + \frac{I_3}{R_y^2}\right)\frac{\partial^2 u_0}{\partial t^2} - \left(I_1 + \frac{I_2}{R_x}\right)\frac{\partial^3 w_0}{\partial x\partial t^2} + \left(I_3 + \frac{I_4}{R_x}\right)\frac{\partial^2\psi_x}{\partial t^2}\right]\end{aligned} \tag{44}$$

$$\begin{aligned}[1-\lambda\nabla^2]\Big[& (A_{12}+A_{66})\frac{\partial^2 u_0}{\partial x\partial y} + A_{22}\frac{\partial^2 v_0}{\partial y^2} + A_{66}\frac{\partial^2 v_0}{\partial x^2} - (B_{12}+2B_{66})\frac{\partial^3 w_0}{\partial x^2\partial y} - B_{22}\frac{\partial^3 w_0}{\partial y^3} + \left(\frac{A_{12}}{R_x} + \frac{A_{22}}{R_y}\right)\frac{\partial w_0}{\partial x} + (B_{12}^s + B_{66}^s)\frac{\partial^2\psi_y}{\partial x\partial y} \\ & + B_{22}^s\frac{\partial^2\psi_y}{\partial y^2} + B_{66}^s\frac{\partial^2\psi_y}{\partial x^2}\Big] = [1-\mu\nabla^2]\left[\left(I_0 + 2\frac{I_1}{R_x} + \frac{I_2}{R_y^2}\right)\frac{\partial^2 v_0}{\partial t^2} - \left(I_1 + \frac{I_2}{R_y}\right)\frac{\partial^3 w_0}{\partial y\partial t^2} + \left(I_3 + \frac{I_4}{R_y}\right)\frac{\partial^2\psi_y}{\partial t^2}\right]\end{aligned} \tag{45}$$

$$\begin{aligned}[1-\lambda\nabla^2]\Big[& B_{11}\frac{\partial^3 u_0}{\partial x^3} + (B_{12}+2B_{66})\frac{\partial^3 u_0}{\partial x\partial y^2} - \left(\frac{A_{11}}{R_x} + \frac{A_{12}}{R_y}\right)\frac{\partial u_0}{\partial x} + (B_{12}+2B_{66})\frac{\partial^3 v_0}{\partial x^2\partial y} + B_{22}\frac{\partial^3 v_0}{\partial y^3} - \left(\frac{A_{12}}{R_x} + \frac{A_{22}}{R_y}\right)\frac{\partial v_0}{\partial y} \\ & + \left(\frac{2B_{11}}{R_x} + \frac{2B_{12}}{R_y}\right)\frac{\partial^2 w_0}{\partial x^2} - D_{11}\frac{\partial^4 w_0}{\partial x^4} - (2D_{12}+4D_{66})\frac{\partial^4 w_0}{\partial x^2\partial y^2} - D_{22}\frac{\partial^4 w_0}{\partial y^4} + \left(\frac{2B_{12}}{R_x} + \frac{2B_{22}}{R_y}\right)\frac{\partial^2 w_0}{\partial y^2} \\ & - \left(\frac{A_{11}}{R_x^2} + 2\frac{A_{12}}{R_xR_y} + \frac{A_{22}}{R_y^2}\right)w_0 + D_{11}^s\frac{\partial^3\psi_x}{\partial x^3} + (D_{12}^s + 2D_{66}^s)\frac{\partial^3\psi_x}{\partial x\partial y^2} - \left(\frac{B_{11}^s}{R_x} + \frac{B_{12}^s}{R_y}\right)\frac{\partial\psi_x}{\partial x} + (D_{12}^s + 2D_{66}^s)\frac{\partial^3\psi_y}{\partial x^2\partial y} \\ & + D_{22}^s\frac{\partial^3\psi_y}{\partial y^3} - \left(\frac{B_{12}^s}{R_x} + \frac{B_{22}^s}{R_y}\right)\frac{\partial\psi_y}{\partial y}\Big] + [1-\mu\nabla^2]\left[-K_w w_0 + K_s\left(\frac{\partial^2 w_0}{\partial x^2} + \frac{\partial^2 w_0}{\partial y^2}\right)\right] \\ & = [1-\mu\nabla^2]\left[I_0\frac{\partial^2 w_0}{\partial t^2} + \left(I_1 + \frac{I_2}{R_x}\right)\frac{\partial^3 u_0}{\partial x\partial t^2} + \left(I_1 + \frac{I_2}{R_y}\right)\frac{\partial^3 v_0}{\partial y\partial t^2} - I_2\left(\frac{\partial^4 w_0}{\partial x^2\partial t^2} + \frac{\partial^4 w_0}{\partial y^2\partial t^2}\right) + I_4\left(\frac{\partial^3\psi_x}{\partial x\partial t^2} + \frac{\partial^3\psi_y}{\partial y\partial t^2}\right)\right]\end{aligned} \tag{46}$$

$$\begin{aligned}[1-\lambda\nabla^2]\Big[& B_{11}^s\frac{\partial^2 u_0}{\partial x^2} + B_{66}^s\frac{\partial^2 u_0}{\partial y^2} + (B_{12}^s + B_{66}^s)\frac{\partial^2 v_0}{\partial x\partial y} - D_{11}^s\frac{\partial^3 w_0}{\partial x^3} - (D_{12}^s + 2D_{66}^s)\frac{\partial^3 w_0}{\partial x\partial y^2} + \left(\frac{B_{11}^s}{R_x} + \frac{B_{12}^s}{R_y}\right)\frac{\partial w_0}{\partial x} + F_{11}^s\frac{\partial^2\psi_x}{\partial x^2} + F_{66}^s\frac{\partial^2\psi_x}{\partial y^2} \\ & - A_{44}^s\psi_x + (F_{12}^s + F_{66}^s)\frac{\partial^2\psi_y}{\partial x\partial y}\Big] = [1-\mu\nabla^2]\left[\left(I_3 + \frac{I_4}{R_x}\right)\frac{\partial^2 u_0}{\partial t^2} - I_4\frac{\partial^3 w_0}{\partial x\partial t^2} + I_5\frac{\partial^2\psi_x}{\partial t^2}\right]\end{aligned} \tag{47}$$

$$\begin{aligned}[1-\lambda\nabla^2]\Big[& (B_{12}^s + B_{66}^s)\frac{\partial^2 u_0}{\partial x\partial y} + B_{11}^s\frac{\partial^2 v_0}{\partial y^2} + B_{66}^s\frac{\partial^2 v_0}{\partial x\partial y} - (D_{12}^s + 2D_{66}^s)\frac{\partial^3 w_0}{\partial x^2\partial y} - D_{22}^s\frac{\partial^3 w_0}{\partial y^3} + \left(\frac{B_{12}^s}{R_x} + \frac{B_{22}^s}{R_y}\right)\frac{\partial w_0}{\partial x} + (F_{12}^s + F_{66}^s)\frac{\partial^2\psi_x}{\partial x\partial y} \\ & + F_{11}^s\frac{\partial^2\psi_y}{\partial y^2} - A_{44}^s\psi_y + F_{66}^s\frac{\partial^2\psi_y}{\partial x^2}\Big] = [1-\mu\nabla^2]\left[\left(I_3 + \frac{I_4}{R_y}\right)\frac{\partial^2 v_0}{\partial t^2} - I_4\frac{\partial^3 w_0}{\partial y\partial t^2} + I_5\frac{\partial^2\psi_y}{\partial t^2}\right]\end{aligned} \tag{48}$$

5. Analytical Solution

This research aims to expand the use of analytical solutions to analyse the response of different structures, including shells, under various boundary conditions. While numerical techniques such as the Finite Element Method (FEM) are highly versatile, this

study employs an analytical solution based on the Galerkin approach to obtain precise solutions. The advantages of this approach include its mathematical simplicity, its ability to satisfy various boundary conditions, and its rapid computation compared to FEM. This extreme efficiency is critical for the present study, as utilizing FEM to generate the more than 100,000 distinct parametric samples required for the machine learning dataset would be exceedingly difficult and computationally prohibitive. The analytical framework is highly effective and reliable for simple continuous structures with uniform thickness, such as beams, plates, and canonical shells (e.g., cylindrical, spherical, conical). Its primary limitation, however, is its restriction to these regular geometries, whereas numerical approaches like FEM remain necessary for analyzing arbitrarily complex shapes or non-uniform features. The generalized displacements can be represented as follows [51]:

$$\begin{aligned}\{u_0,\psi_x\} &= \sum_{m=1}^{\infty}\sum_{n=1}^{\infty}\{U_{mn},X_{mn}\}\frac{\partial X_m(x)}{\partial x}Y_n(y)e^{i\omega t}\\ \{v_0,\psi_y\} &= \sum_{m=1}^{\infty}\sum_{n=1}^{\infty}\{V_{mn},Z_{mn}\}X_m(x)\frac{\partial Y_n(y)}{\partial y}e^{i\omega t}\\ w_0 &= \sum_{m=1}^{\infty}\sum_{n=1}^{\infty}W_{mn}X_m(x)Y_n(y)\,e^{i\omega t}\end{aligned} \tag{49}$$

where U_{mn}, V_{mn}, W_{mn}, $X_{mn}$and Z_{mn} are arbitrary parameters. The Galerkin solution requires admissible functions $X_m(x)$ and $Y_n(y)$ that satisfy the geometric (essential) boundary conditions along the four edges of the doubly-curved nanoshell. In the present study, three sets of boundary conditions are considered:

- Simply supported (SSSS) on all four edges:

$$\begin{aligned}v_0 = w_0 = \psi_y = 0 \quad \text{at} \quad x = 0, a\\ u_0 = w_0 = \psi_x = 0 \quad \text{at} \quad y = 0, b\end{aligned} \tag{50}$$

- Clamped (CCCC) on all four edges:

$$u_0 = v_0 = w_0 = \psi_x = \psi_y = 0 \quad \text{at} \quad x = 0, a \quad \text{and} \quad y = 0, b \tag{51}$$

- Simply supported–clamped (SCSC):

$$\begin{aligned}v_0 = w_0 = \psi_y = 0 \quad \text{at} \quad x = 0, a\\ u_0 = v_0 = w_0 = \psi_x = \psi_y = 0 \quad \text{at} \quad y = 0, b\end{aligned} \tag{52}$$

Table 2 contains the functions $X_m(x)$ and $Y_n(y)$ that satisfy the above boundary conditions. By substituting Eq. (48) in Eqs. (43-47), one obtains:

$$([K]-\omega_{mn}^2\,[M])\begin{Bmatrix}U_{mn}\\V_{mn}\\W_{mn}\\X_{mn}\\Z_{mn}\end{Bmatrix}=0 \tag{53}$$

where $[K]$ and $[M]$ are the rigidity matrix and mass matrix, respectively. The elements K_{ij} and M_{ij} of the matrix $[K]$ and $[M]$ are given in Appendix A.

6. Results and Discussion

The composite shell under analysis comprises a mixture of armchair (10,10) single-walled CNTs and a polymer matrix. The material properties of the polymer are reported as $E_p = 2.5$ GPa, $\rho_p = 1190$ kg/m^3 and $\upsilon_p = 0.19$, as per Tornabene et al. [17]. The density of CNTs is assumed to be$\rho_f = 1400$ kg/m^3.

The normalized results for frequencies are converted to the following forms:

$$\bar{\omega} = 10^2 h\sqrt{\frac{\rho_m}{E_m}}\omega \tag{54}$$

The foundation stiffnesses are expressed in dimensionless form as:

$$K_w = \frac{k_w a^2}{D}, \qquad K_s = \frac{k_s}{D} \tag{55}$$

where $D = \frac{E_2 h^3}{12(1-\upsilon_{12}{}^2)}$.

6.1. Verification analysis

To validate the proposed mathematical formulation, Table 3 presents a comparative analysis of the natural circular frequencies (rad/s) for a simply supported isotropic homogeneous spherical shell. The geometric dimensions of the selected shell are defined as $a = b = 1.0118\,m$, with a thickness of $h = 0.0191\ m$ and a constant radius of curvature $R = 1.91\ m$. The mechanical properties of the material are set to Young's modulus $E = 1$ Pa , mass density $\rho = 1$ kg/m^3, and Poisson's ratio $\nu = 0.3$.

Table 2. The admissible functions $X_m(x)$ and $Y_n(y)$.

BCs	The functions X_m and Y_n	
	$X_m(x)$	$Y_n(y)$
SSSS	$\sin(\alpha x)$	$\sin(\beta y)$
CCCC	$\sin^2(\alpha x)$	$\sin^2(\beta y)$
SCSC	$\sin(\alpha x)[\cos(\alpha x)-1]$	$\sin(\beta y)[\cos(\beta y)-1]$

where $\alpha = m\pi/a$, $\beta = n\pi/b$, m and n are mode numbers.

Table 3. Comparison of natural circular frequencies (rad/s) for isotropic homogeneous spherical shells.

m, n	Present	Jouneghani et al. [55]	Fadaee et al. [53]	Vinh et al. [54]	Khare et al. [52]
(1, 1)	0.52870	0.52692	0.52864	0.52830	0.50211
(2, 1)	0.58940	0.58120	0.58954	0.58853	0.56247
(1, 2)	0.58908	0.58120	0.58954	0.58853	0.56248
(2, 2)	0.68251	0.66757	0.68370	0.68231	0.65706
(3, 1)	0.75952	0.73173	0.75974	0.75818	0.73915
(1, 3)	0.75735	0.73173	0.75974	0.75818	0.74035
(3, 2)	0.88472	0.87284	0.88680	0.88507	0.86359
(2, 3)	0.88205	0.87284	0.88680	0.88507	0.86360

Table 4. Validation of the natural frequency parameter $(\tilde{\omega} = \omega h\sqrt{\rho_c/E_c})$ for fully simply supported Al/Al_2O_3 FG square plates and doubly-curved shells against literature ($a = b = 10h$, $m = n = 1$).

$\frac{a}{R_x}$	$\frac{b}{R_y}$	p	Present	Matsunaga [48]	Chorfi & Houmat [56]	Alijani et al. [57]	Trinh & Kim [58]
0.5	0.5	0	0.0753	0.0751	0.0762	0.0779	0.0761
		1	0.0595	0.0601	0.0607	0.0617	0.0605
		4	0.0496	0.0503	0.0509	0.0519	0.0506
		10	0.0459	0.0464	0.0471	0.0482	0.0467
0.5	0	0	0.0622	0.0622	0.0629	0.0648	0.0628
		1	0.0482	0.0485	0.0490	0.0501	0.0488
		4	0.0410	0.0413	0.0419	0.0430	0.0416
		10	0.0387	0.0390	0.0395	0.0408	0.0392
0.5	-0.5	0	0.0563	0.0563	0.0580	0.0597	0.0577
		1	0.0431	0.0432	0.0445	0.0456	0.0442
		4	0.0371	0.0372	0.0385	0.0396	0.0381
		10	0.0354	0.0355	0.0368	0.0380	0.0364
0	0	0	0.0577	0.0588	0.0577	0.0597	0.0577
		1	0.0442	0.0430	0.0442	0.0456	0.0442
		4	0.0380	0.0381	0.0383	0.0396	0.0381
		10	0.0363	0.0364	0.0366	0.0380	0.0364

The present frequencies, derived using HSDT solved via the Galerkin analytical method, are compared against several established numerical and analytical solutions in the literature. These reference studies encompass a variety of theoretical frameworks, including HSDT combined with FEM by Khare et al. [52], FSDT and FEM models by Fadaee et al. [53], as well as FSDT models solved using Navier's analytical technique by Vinh et al. [54] and Jouneghani et al. [55].

As detailed in Table 3, the analysis spans the fundamental mode $(1,1)$ through higher-order mode shapes up to $(3,2)$ and $(2,3)$. The present HSDT-Galerkin methodology demonstrates excellent agreement with the comparative literature solutions across all evaluated modes.

The accuracy of the proposed HSDT formulation and analytical solution is validated also by comparing the computed natural frequencies of functionally graded shells with published literature (Table 4). The analysis employed a standard Alumina/Aluminum (Al_2O_3/Al) composite, utilizing $E_c = 380$ GPa, $\rho_c = 3800$ kg/m³ for the ceramic, and $E_m = 70$ GPa, $\rho_m = 2707$ kg/m³ for the metal, assuming a uniform Poisson's ratio ($\nu = 0.3$). The model shows excellent agreement with benchmark solutions across all configurations, with deviations within 1–2%. This precision validates the framework for the ensuing parametric analysis of FG-CNT nanoshells.

6.2. Effect of material properties

Figures 4 and 5 illustrate how variations in agglomeration parameters affect Young's modulus and Poisson's ratio, as shown in the graphs. It can be observed that Young's modulus reaches its highest values when ζ equals ξ. Additionally, it is noticeable that the elastic properties are more significantly impacted by the variation of the ξ parameter compared to ζ.

The influences of various material parameters, such as inhomogeneity parameters p, k and e, CNTs agglomeration parameters ζ and ξ and CNTs volume fraction V_{cnt} is examined in Tables 5-7 and Figs. 6-10.

Table 5 investigates the effect of changes in the inhomogeneity parameters p, k, and e on the dimensionless frequency $\bar{\omega}$ of coated spherical FG CNTs shells, where $R_x/a = R_y/b = 5$. The table covers different types and designs of FG coated shells.

In Table 6, the effect of a change in volume fraction V_{cnt} on the dimensionless frequency $\bar{\omega}$ of various types of coated spherical FG CNTs shells is illustrated. The volume fraction V_{cnt} is changed from 0% to 1%. Dimensionless frequencies $\bar{\omega}$ of coated FG CNTs nanoshells versus CNTs agglomeration parameters ζ and ξ are tabulated in Table 7. The CNTs agglomeration parameter ζ is changed from 0 to 1, while the parameter ξ is changed from 0.1 to 0.9. Figures 6-10 have been plotted to provide further detail.

Figure 6 displays the dimensionless frequencies of FG-A CNTs shell as a function of the material distribution indexes p, k, and e ($p, k, e = 0\sim10$). For hardcore FG structures, increasing the indexes p, k, and e increases the dimensionless frequency. Conversely, for softcore FG structures, the dimensionless frequencies decrease as the inhomogeneity indexes increase. When the hardcore shell indexes p, k, and e equal to 0, the shell is entirely polymer, and for the case of the softcore shell with indexes p, k, and e equal to 0, the shell is uniformly CNTs distributed.

Table 5. Dimensionless frequency $\bar{\omega}$ of coated FG CNTs shells versus exponents p, k and e $(SSSS, R_x/a = R_y/b = 5, b = a = 10h, \zeta = 1, \xi = 0.5,\ \mu = \lambda = K_w = K_s = 0)$.

p	k	p	Hardcore					Softcore				
			FG-A	FG-B	FG-C	FG-D	FG-E	FG-A	FG-B	FG-C	FG-D	FG-E
0	0	0	5.9728	5.9728	5.9728	5.9728	5.9728	7.3994	7.3994	7.3994	7.3994	7.3994
2	2	2	6.2801	6.6454	6.4275	6.6420	6.9570	7.1397	6.803	7.0054	6.7976	6.4839
		5	6.3543	6.8030	6.4275	6.6420	6.9570	7.0730	6.6454	7.0054	6.7976	6.4839
		10	6.3877	6.8734	6.4275	6.6420	6.9570	7.0424	6.5725	7.0054	6.7976	6.4839
	5	2	6.3543	6.8030	6.5357	6.6420	7.1816	7.0730	6.6454	6.9025	6.7976	6.2337
		5	6.4457	6.9949	6.5357	6.6420	7.1816	6.9884	6.4429	6.9025	6.7976	6.2337
		10	6.4868	7.0804	6.5357	6.6420	7.1816	6.9495	6.3486	6.9025	6.7976	6.2337
	10	2	6.3877	6.8734	6.5843	6.6420	7.2814	7.0424	6.5725	6.8551	6.7976	6.1165
		5	6.4868	7.0804	6.5843	6.6420	7.2814	6.9495	6.3486	6.8551	6.7976	6.1165
		10	6.5313	7.1725	6.5843	6.6420	7.2814	6.9068	6.2442	6.8551	6.7976	6.1165
5	2	2	6.4234	6.6454	6.6367	6.9440	6.9570	7.0120	6.8030	6.8094	6.4926	6.4839
		5	6.5310	6.8030	6.6367	6.9440	6.9570	6.9115	6.6454	6.8094	6.4926	6.4839
		10	6.5793	6.8734	6.6367	6.9440	6.9570	6.8653	6.5725	6.8094	6.4926	6.4839
	5	2	6.5310	6.8030	6.7922	6.9440	7.1816	6.9115	6.6454	6.6531	6.4926	6.2337
		5	6.6629	6.9949	6.7922	6.9440	7.1816	6.7836	6.4429	6.6531	6.4926	6.2337
		10	6.7220	7.0804	6.7922	6.9440	7.1816	6.7246	6.3486	6.6531	6.4926	6.2337
	10	2	6.5793	6.8734	6.8616	6.9440	7.2814	6.8653	6.5725	6.5807	6.4926	6.1165
		5	6.7220	7.0804	6.8616	6.9440	7.2814	6.7246	6.3486	6.5807	6.4926	6.1165
		10	6.7858	7.1725	6.8616	6.9440	7.2814	6.6596	6.2442	6.5807	6.4926	6.1165
10	2	2	6.5106	6.6454	6.7631	7.1246	6.9570	6.9317	6.803	6.6852	6.2966	6.4839
		5	6.6380	6.8030	6.7631	7.1246	6.9570	6.8096	6.6454	6.6852	6.2966	6.4839
		10	6.6952	6.8734	6.7631	7.1246	6.9570	6.7533	6.5725	6.6852	6.2966	6.4839
	5	2	6.6380	6.8030	6.9463	7.1246	7.1816	6.8096	6.6454	6.4939	6.2966	6.2337
		5	6.7939	6.9949	6.9463	7.1246	7.1816	6.6537	6.4429	6.4939	6.2966	6.2337
		10	6.8636	7.0804	6.9463	7.1246	7.1816	6.5816	6.3486	6.4939	6.2966	6.2337
	10	2	6.6952	6.8734	7.0279	7.1246	7.2814	6.7533	6.5725	6.4050	6.2966	6.1165
		5	6.8636	7.0804	7.0279	7.1246	7.2814	6.5816	6.3486	6.4050	6.2966	6.1165
		10	6.9388	7.1725	7.0279	7.1246	7.2814	6.5019	6.2442	6.4050	6.2966	6.1165

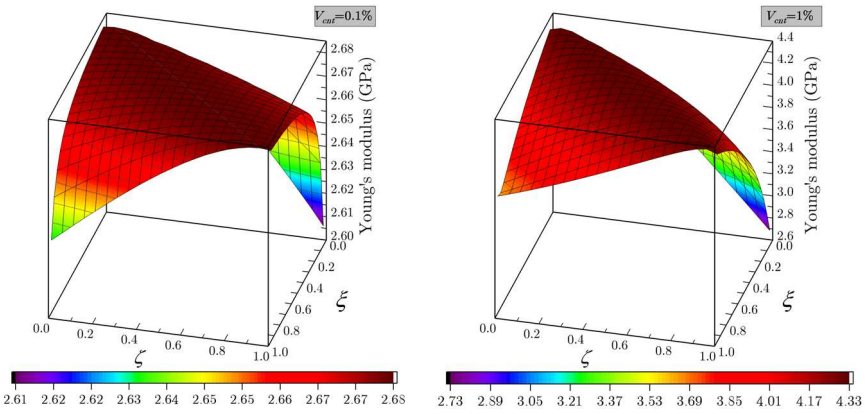


Fig. 4. Young's modulus influenced by the agglomeration parameters ζ and ξ.

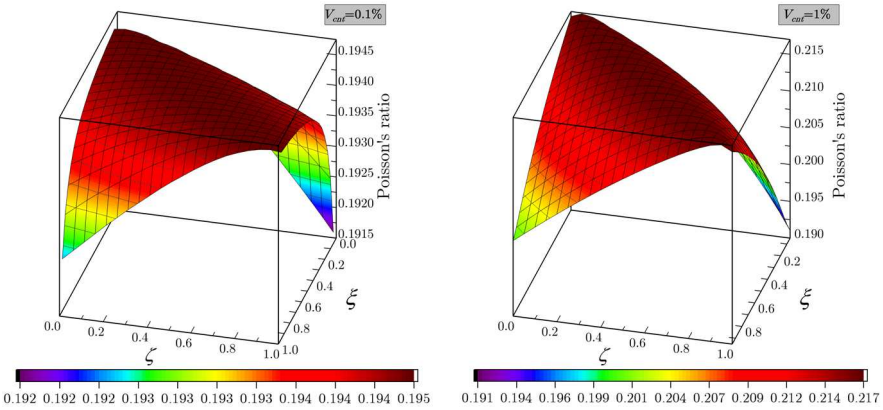


Fig. 5. Poisson's ratio influenced by the agglomeration parameters ζ and ξ.

Table 6. Dimensionless frequency $\bar{\omega}$ of coated FG CNTs shells versus the CNTs volume fraction V_{cnt} $(SSSS, p=k=e=2, b=a=10h, \zeta=1, \xi=0.5, \mu=\lambda=K_w=K_s=0)$.

V_{cnt}	Hardcore					Softcore				
	FG-A	FG-B	FG-C	FG-D	FG-E	FG-A	FG-B	FG-C	FG-D	FG-E
0.0%	5.9573	5.9573	5.9573	5.9573	5.9573	5.9573	5.9573	5.9573	5.9573	5.9573
0.2%	6.0432	6.1407	6.0824	6.1406	6.2272	6.2793	6.1841	6.2412	6.1836	6.0970
0.4%	6.1157	6.2956	6.1881	6.2949	6.4531	6.5471	6.3748	6.4783	6.3733	6.2153
0.6%	6.1780	6.4285	6.2789	6.4269	6.6455	6.7742	6.5379	6.6798	6.5351	6.3171
0.8%	6.2323	6.5440	6.3580	6.5415	6.8118	6.9695	6.6792	6.8537	6.6751	6.4058
1.0%	6.2801	6.6454	6.4275	6.6420	6.9570	7.1397	6.8030	7.0054	6.7976	6.4839

Table 7. Dimensionless frequency $\bar{\omega}$ of coated FG CNTs nanoshells versus CNTs agglomeration parameters ζ and ξ $(SSSS, p=k=2,\ R_x/a=R_y/b=5, b=a=10h,\ \mu=\lambda=K_w=K_s=0)$.

ζ	ξ	Hardcore					Softcore				
		FG-A	FG-B	FG-C	FG-D	FG-E	FG-A	FG-B	FG-C	FG-D	FG-E
0.0	0.1	6.3852	6.8577	6.5765	6.8528	7.2556	7.4866	7.0595	7.3162	7.0502	6.6497
	0.2	6.3717	6.8307	6.5575	6.8260	7.2179	7.4430	7.0270	7.2770	7.0182	6.6285
	0.5	6.3216	6.7302	6.4868	6.7262	7.0768	7.2793	6.9057	7.1302	6.8988	6.5499
	0.9	6.2287	6.5416	6.3548	6.5388	6.8101	6.9685	6.6772	6.8524	6.6734	6.4030
0.1	0.1	6.3974	6.8821	6.5938	6.8770	7.2896	7.5261	7.0888	7.3516	7.0790	6.6688
	0.2	6.3914	6.8700	6.5853	6.8650	7.2728	7.5066	7.0743	7.3340	7.0647	6.6594
	0.5	6.3473	6.7816	6.5230	6.7773	7.1490	7.3631	6.9678	7.2054	6.9600	6.5901
	0.9	6.2505	6.5855	6.3856	6.5825	6.8724	7.0411	6.7305	6.9173	6.7261	6.4372
0.2	0.1	6.3887	6.8646	6.5815	6.8597	7.2652	7.4978	7.0678	7.3262	7.0584	6.6552
	0.2	6.3974	6.8821	6.5938	6.8770	7.2896	7.5261	7.0888	7.3516	7.0790	6.6688
	0.5	6.3682	6.8236	6.5526	6.8190	7.2078	7.4313	7.0184	7.2665	7.0097	6.6230
	0.9	6.2723	6.6296	6.4165	6.6263	6.9347	7.1138	6.7839	6.9822	6.7788	6.4716
0.5	0.1	6.2999	6.6833	6.4548	6.6797	7.0097	7.2007	6.8485	7.0602	6.8424	6.5139
	0.2	6.3532	6.7927	6.5310	6.7884	7.1643	7.3807	6.9810	7.2212	6.9730	6.5990
	0.5	6.3974	6.8821	6.5938	6.8770	7.2896	7.5261	7.0888	7.3516	7.0790	6.6688
	0.9	6.3366	6.7596	6.5077	6.7554	7.1178	7.3268	6.9410	7.1729	6.9336	6.5730
1.0	0.1	6.0593	6.1825	6.1085	6.1813	6.2908	6.3563	6.2369	6.3089	6.2370	6.1276
	0.2	6.1361	6.3464	6.2205	6.3447	6.5294	6.6386	6.4386	6.5590	6.4373	6.2529
	0.5	6.2801	6.6454	6.4275	6.6420	6.9570	7.1397	6.8030	7.0054	6.7976	6.4839
	0.9	6.3803	6.8480	6.5697	6.8432	7.2420	7.4710	7.0478	7.3021	7.0387	6.6421

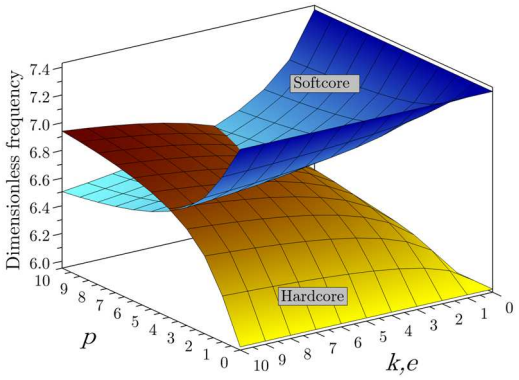


Fig. 6. Effect of the exponents p, k and e on the dimensionless frequencies of various types of CNTs coated shell $(SSSS, b=a=10h, \zeta=1, \xi=0.5, R_x/a=R_y/b=5)$.

The effect of the volume fraction V_{cnt} by considering various values of agglomeration parameters ξ $(\xi=0.1,0.5,0.7,0.9)$ and $(\zeta=0,0.2,0.5,0.7,1)$ on the dimensionless frequencies of FG-A CNTs coated shell is plotted in Figs. 7 and 8, respectively. The increase in the volume fraction of CNTs results in an improvement in the shell's rigidity, leading to an increase in the dimensionless frequencies for all types of CNTs FG shells. In addition, the increase of the agglomeration parameters ξ leads to an increment in the shell rigidity and the dimensionless frequencies, while for values of agglomeration parameters $\zeta \leq 0.5$ the dimensionless frequencies increase, and decrease for values $\zeta \geq 0.5$, and this can be explained by the variation of young's modulus as plotted in Fig. 4.

Other curves are plotted in Figs. 9 and 10 to show the action of both agglomeration parameters ξ and ζ by considering the power-law indexes and the FG CNTs distribution patterns. It is clear that, unlike the softcore shells, shell rigidity and dimensionless frequencies increase with increasing power-law indexes for the Hardcore shells. For the Hardcore CNTs distribution, the rigid shell is the FG-E, while for the softcore shells, the rigid one is the FG-A.

6.3. Effect of the small size and shell geometry

The influences of the radius of curvature R_x/a and R_y/b on the dimensionless frequency $\bar{\omega}$ of coated FG CNTs shells is plotted in Table 8. The vibrational behavior of the same structures is analyzed in Table 9 by considering various boundary conditions, SSSS, CCCC and SCSC.

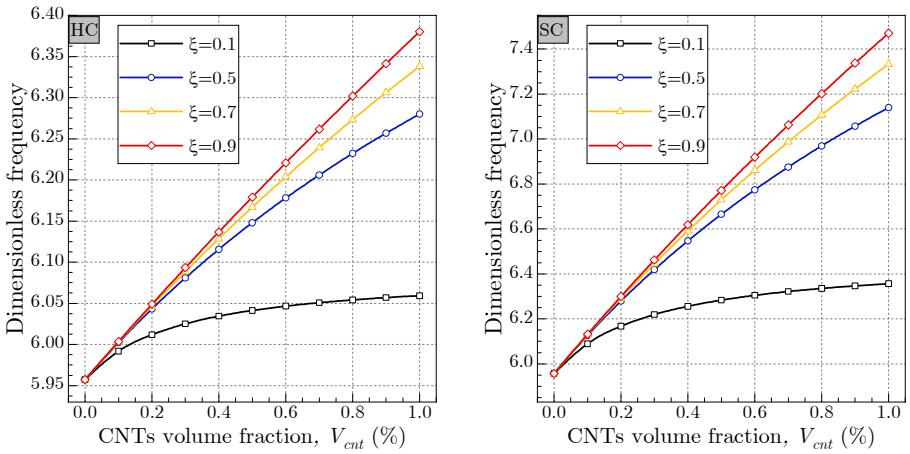


Fig. 7. Effect of the volume fraction V_{cnt} and the agglomeration parameter ξ on the dimensionless frequencies of FG-A CNTs coated shell $(SSSS, p, k, e = 2, b = a = 10h, \zeta = 1, R_x/a = R_y/b = 5)$.

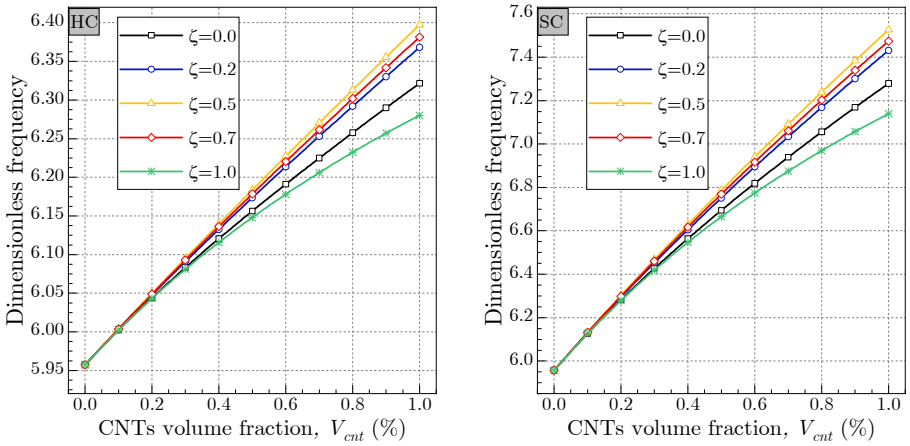


Fig. 8. Effect of the volume fraction V_{cnt} and the agglomeration parameter ζ on the dimensionless frequencies of FG-A CNTs coated shell $(SSSS, p = k = e = 2, b = a = 10h, \xi = 0.5, R_x/a = R_y/b = 5)$.

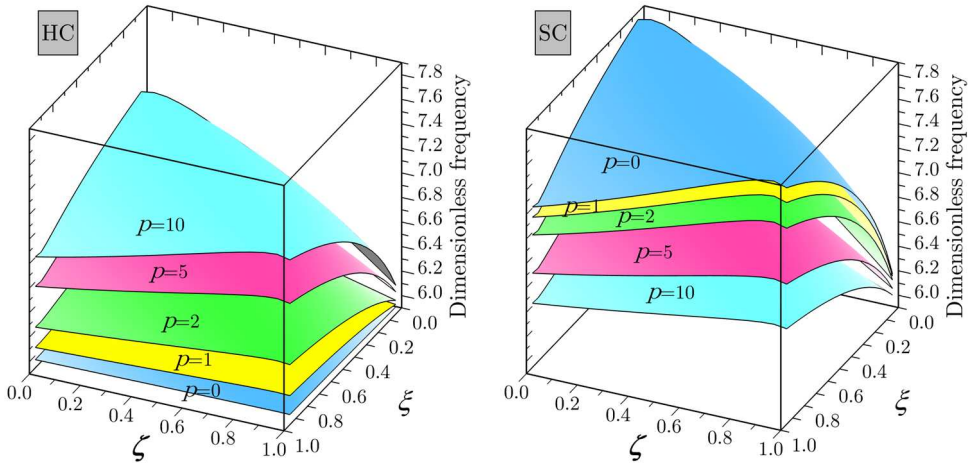


Fig. 9. Effect of the agglomeration parameter ζ and ξ on the dimensionless frequencies of FG-A CNTs coated shell $(SSSS, b = a = 10h, R_x/a = R_y/b = 5)$.

In Figs. 11 and 12, the influence of the nonlocal parameter μ and the length-scale parameter λ on the dimensionless frequencies of hardcore FG-A-coated FG shells. The results indicate that a decrease in the nonlocal parameter μ increases the dimensionless frequencies, implying that the nonlocal effect causes stiffness softening. On the other hand, a decrease in the length-scale parameter λ results in a decrease in the dimensionless frequencies, indicating that the length-scale causes a stiffness-hardening effect. In addition, the dimensionless frequencies increase with the increase in the thickness ratio a/h and by the reduction in the aspect ratio b/a.

Figure 13 illustrates the effect of the radius of curvature R_x/a and R_y/b on the dimensionless frequencies of FG-A CNTs tri-coated shell for a constant inhomogeneity index $p = k = e = 2$. In general, except for the simply supported hyperbolic-paraboloidal shell ($R_x/a = 5$ and $R_y/b = -5$), the augmentation of the radius of curvature R_x/a decreases the dimensionless frequencies. For the values of $R_y/b \geq 10$, the frequencies decrease slowly.

Table 8. Dimensionless frequency $\bar{\omega}$ of coated FG CNTs shells with various geometries $(SSSS, b = a = 10h, \zeta = 1, \xi = 0.5, \mu = \lambda = K_w = K_s = 0)$.

$\frac{R_x}{a}, \frac{R_y}{b}$	$p = k = e$	Hardcore					Softcore				
		FG-A	FG-B	FG-C	FG-D	FG-E	FG-A	FG-B	FG-C	FG-D	FG-E
5, 5	0	5.9728	5.9728	5.9728	5.9728	5.9728	7.3994	7.3994	7.3994	7.3994	7.3994
	2	6.2801	6.6454	6.4275	6.6420	6.9570	7.1397	6.8030	7.0054	6.7976	6.4839
	5	6.6629	6.9949	6.7922	6.9440	7.1816	6.7836	6.4429	6.6531	6.4926	6.2337
	10	6.9388	7.1725	7.0279	7.1246	7.2814	6.5019	6.2442	6.4050	6.2966	6.1165
Inf, 5	0	5.7211	5.7211	5.7211	5.7211	5.7211	7.0875	7.0875	7.0875	7.0875	7.0875
	2	6.0024	6.3653	6.1376	6.3343	6.6638	6.8500	6.5163	6.7273	6.5374	6.2106
	5	6.3671	6.7001	6.4882	6.6306	6.8790	6.5123	6.1713	6.3904	6.2408	5.9709
	10	6.6348	6.8702	6.7191	6.8107	6.9745	6.2401	5.9810	6.1487	6.0465	5.8587
5, -5	0	5.6194	5.6194	5.6194	5.6194	5.6194	6.9616	6.9616	6.9616	6.9616	6.9616
	2	5.8910	6.2522	6.0215	6.2115	6.5453	6.7324	6.4005	6.6140	6.4308	6.1003
	5	6.2484	6.5811	6.3664	6.5051	6.7567	6.4019	6.0617	6.2834	6.1378	5.8648
	10	6.5126	6.7481	6.5952	6.6847	6.8506	6.1337	5.8748	6.0444	5.9446	5.7546
5, 7,5	0	5.8733	5.8733	5.8733	5.8733	5.8733	7.2761	7.2761	7.2761	7.2761	7.2761
	2	6.1703	6.5347	6.3129	6.5204	6.8411	7.0253	6.6897	6.8956	6.6948	6.3759
	5	6.5460	6.8784	6.6720	6.8201	7.0620	6.6764	6.3356	6.5493	6.3932	6.1298
	10	6.8186	7.0530	6.9059	7.0006	7.1602	6.3985	6.1402	6.3038	6.1978	6.0146

Table 9. Dimensionless frequency $\bar{\omega}$ of coated FG CNTs nanoshells versus nonlocal and length-scale parameters$(SSSS, p = k = e = 2,\ R_x/a = R_y/b = 5, b = a = 10h, \zeta = 1, \xi = 0.5, K_w = K_s = 0)$.

BCs	μ	λ	Hardcore					Softcore				
			FG-A	FG-B	FG-C	FG-D	FG-E	FG-A	FG-B	FG-C	FG-D	FG-E
SSSS	0	0	6.2801	6.6454	6.4275	6.6420	6.9570	7.1397	6.8030	7.0054	6.7976	6.4839
		1	6.8927	7.2928	7.0549	7.2908	7.6347	7.8345	7.4657	7.6868	7.4582	7.1155
		2	7.4330	7.8649	7.6078	7.8619	8.2336	8.4495	8.0514	8.2903	8.0440	7.6737
	1	0	5.7391	6.0730	5.8739	6.0699	6.3577	6.5247	6.2170	6.4020	6.2121	5.9254
		1	6.2990	6.6646	6.4472	6.6628	6.9771	7.1597	6.8227	7.0247	6.8157	6.5026
		2	6.7928	7.1874	6.9525	7.1847	7.5244	7.7217	7.3579	7.5762	7.3511	7.0128
	2	0	5.3175	5.6269	5.4424	5.6240	5.8907	6.0454	5.7603	5.9317	5.7557	5.4901
		1	5.8362	6.1750	5.9736	6.1733	6.4646	6.6338	6.3215	6.5087	6.3151	6.0250
		2	6.2938	6.6594	6.4418	6.6570	6.9717	7.1544	6.8174	7.0197	6.8111	6.4976
CCCC	0	0	11.1190	11.7520	11.3840	11.7690	12.3030	12.6100	12.0300	12.3630	11.9760	11.4660
		1	13.8780	14.6720	14.2080	14.6860	15.3600	15.7460	15.0200	15.4370	14.9560	14.3150
		2	16.1510	17.0770	16.5340	17.0880	17.8770	18.3290	17.4820	17.9710	17.4120	16.6620
	1	0	9.8746	10.4370	10.1100	10.4520	10.9260	11.2000	10.6850	10.9800	10.6370	10.1830
		1	12.3260	13.0310	12.6190	13.0430	13.6420	13.9850	13.3400	13.7120	13.2850	12.7140
		2	14.3450	15.1670	14.6840	15.1770	15.8790	16.2800	15.5270	15.9630	15.4660	14.7990
	2	0	8.9722	9.4834	9.1862	9.4964	9.9281	10.1770	9.7083	9.9772	9.6656	9.2529
		1	11.2000	11.8410	11.4660	11.8510	12.3960	12.7080	12.1220	12.4600	12.0720	11.5530
		2	13.0340	13.7820	13.3430	13.7900	14.4280	14.7930	14.1090	14.5050	14.0550	13.4470
CCSS	0	0	10.7190	11.3430	10.9690	11.3330	11.8740	12.1840	11.6120	11.9520	11.5910	11.0670
		1	13.0250	13.7820	13.3300	13.7720	14.4290	14.8040	14.1090	14.5220	14.0820	13.4470
		2	14.9480	15.8190	15.2970	15.8040	16.5600	16.9910	16.1940	16.6680	16.1630	15.4340
	1	0	9.3371	9.8806	9.5554	9.8722	10.3440	10.6140	10.1150	10.4120	10.0980	9.6405
		1	11.3460	12.0060	11.6120	11.9970	12.5690	12.8960	12.2910	12.6510	12.2680	11.7150
		2	13.0220	13.7800	13.3260	13.7670	14.4260	14.8020	14.1070	14.5200	14.0810	13.4450
	2	0	8.3810	8.8689	8.5769	8.8612	9.2847	9.5268	9.0792	9.3457	9.0637	8.6533
		1	10.1850	10.7770	10.4230	10.7680	11.2820	11.5760	11.0330	11.3550	11.0120	10.5150
		2	11.6890	12.3690	11.9620	12.3580	12.9490	13.2870	12.6630	13.0340	12.6390	12.0690

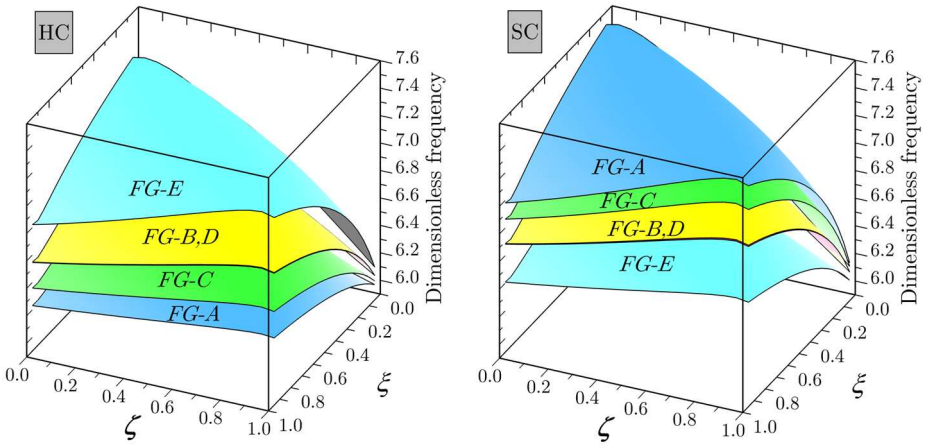


Fig. 10. Effect of the agglomeration parameter ζ and ξ on the dimensionless frequencies of various types of FG CNTs coated shell $(SSSS, p, k, e = 2, b = a = 10h, R_x/a = R_y/b = 5)$.

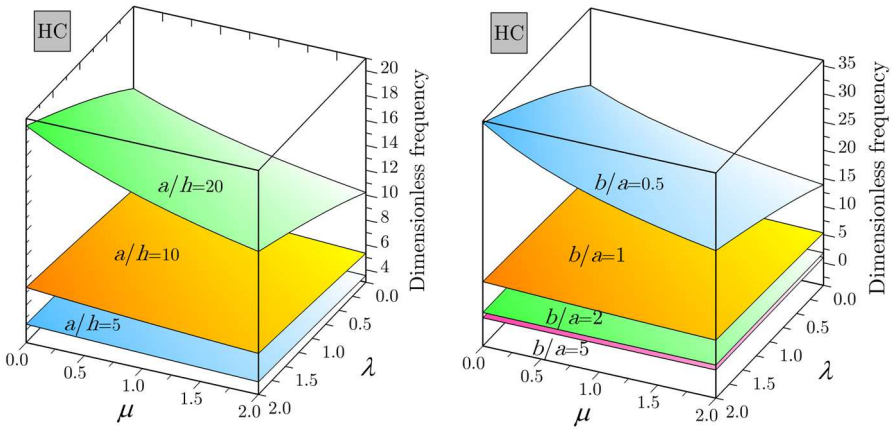


Fig. 11. Effect of nonlocal and length-scale parameters, aspect ratio and thickness ratio on the dimensionless frequencies of FG-A CNTs coated shell $(SSSS, p = k = e = 2, R_x/a = R_y/b = 5, \zeta = 1, \xi = 0.5)$.

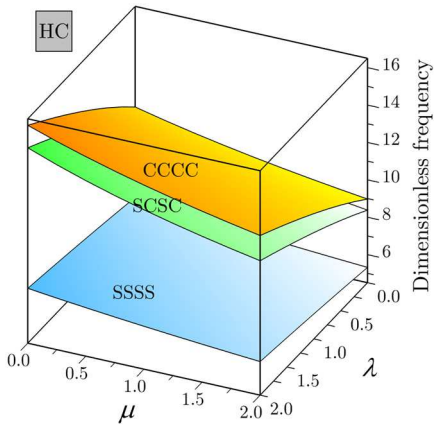


Fig. 12. Effect of nonlocal and length-scale parameters and boundary conditions on the dimensionless frequencies of FG-A coated shell $(SSSS, p = k = e = 2, b = a = 10h, R_x/a = 5, R_y/b = 5, \zeta = 1, \xi = 0.5)$.

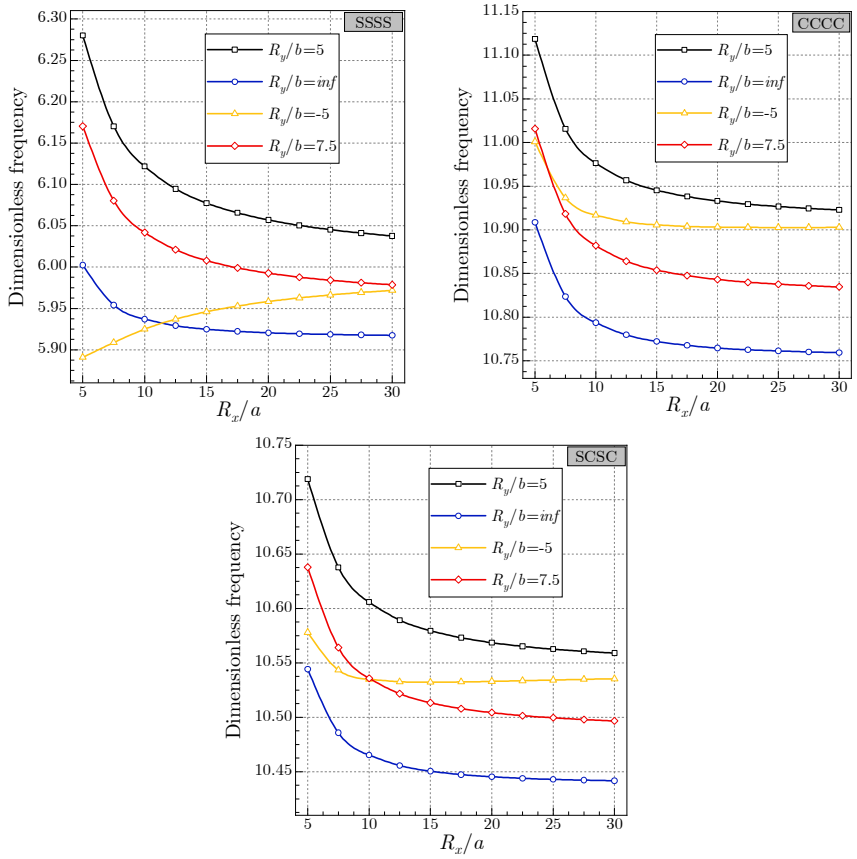


Fig. 13. Effect of the radius of curvature on the dimensionless frequencies of FG-A coated shell $(SSSS, p = k = e = 2, b = a = 10h, \zeta = 1, \xi = 0.5)$.

Table 10. Dimensionless frequency $\bar{\omega}$ of coated FG CNTs shells versus elastic foundation parameters $(SSSS, p = 2,\ R_x/a = R_y/b = 5, b = a = 10h, \zeta = 1, \xi = 0.5,\ \mu = \lambda = 0)$.

K_W	K_S	Hardcore					Softcore				
		FG-A	FG-B	FG-C	FG-D	FG-E	FG-A	FG-B	FG-C	FG-D	FG-E
100	10	6.9272	7.2599	7.0609	7.2564	7.5459	7.7147	7.4043	7.5908	7.3997	7.1125
	50	9.4951	9.7402	9.5925	9.7364	9.9544	10.0830	9.8479	9.9892	9.8459	9.6312
	100	11.5032	11.7060	11.5832	11.7018	11.8842	11.9922	11.7955	11.9140	11.7949	11.6159
500	10	9.0647	9.3212	9.1668	9.3174	9.5450	9.6790	9.4338	9.5811	9.4313	9.2072
	50	11.1506	11.3598	11.2332	11.3557	11.5435	11.6546	11.4520	11.5740	11.4512	11.2668
	100	12.9034	13.0844	12.9744	13.0799	13.2435	13.3406	13.1642	13.2707	13.1645	13.0040
1000	10	11.1755	11.3843	11.2580	11.3801	11.5675	11.6785	11.4763	11.5980	11.4755	11.2915
	50	12.9249	13.1056	12.9958	13.1011	13.2645	13.3615	13.1853	13.2917	13.1857	13.0254
	100	14.4640	14.6256	14.5270	14.6207	14.7676	14.8548	14.6968	14.7925	14.6979	14.5540

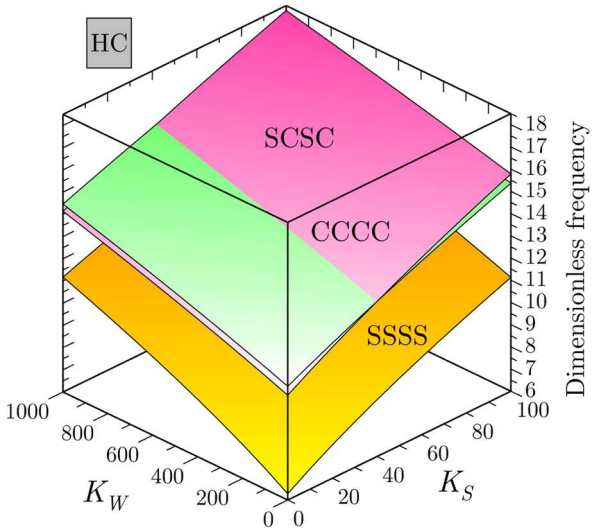


Fig. 14. Effect of the elastic foundation parameters on the dimensionless frequencies of FG-A coated shell $(SSSS, p = k = e = 2, b = a = 10h, R_x/a = 5, R_y/b = 5, \zeta = 1, \xi = 0.5)$.

6.4. Effect of the Winkler and Pasternak foundation

The following analysis is focused on the impact of the Winkler and Pasternak parameters on the dimensionless frequency of various types of coated FG CNTs shells. Table 10 shows a numerical result, where the Winkler parameter is taken as $K_W = 100, 500$ and 1000, while the Pasternak (shear) parameter is taken as $K_S = 10, 50$ and 100. These results are translated into Fig. 14. Both the increase of Winkler parameter K_W and Pasternak parameter K_S increase the dimensionless frequency.

7. Machine Learning-Based Prediction of Vibration Frequencies

The analytical model presented in the previous sections provides highly accurate solutions for the free vibration analysis of coated functionally graded carbon nanotube (FG-CNT) nanoshells. Nevertheless, repeated analytical computations become computationally expensive when large parametric studies, optimization procedures, uncertainty analyses, or real-time structural assessments are required. To overcome this limitation, a machine learning (ML) surrogate model based on Random Forest (RF) regression is developed to predict the normalized fundamental frequencies directly from the governing structural and material parameters.

Random Forest is an ensemble learning algorithm that combines multiple regression decision trees through bootstrap aggregation (bagging). Owing to its capability of learning highly nonlinear relationships without requiring an explicit mathematical model, RF is particularly suitable for complex mechanics problems involving strong interactions among geometric, material, and agglomeration parameters.

7.1. Dataset generation

The dataset used to train and validate the RF model was generated entirely from the analytical Galerkin solution developed in this work. Consequently, every sample corresponds to an exact analytical solution obtained from the governing equations, ensuring complete consistency between the physics-based model and the machine-learning framework.

The generated database covers the entire design space by considering both Hardcore and Softcore material schemes together with the five coated FG distribution patterns (FG-A, FG-B, FG-C, FG-D and FG-E). The material grading indices vary as $p = 0{:}\,2{:}\,10$, $k = 0{:}\,2{:}\,10$, $e = 0{:}\,2{:}\,10$, while the CNT agglomeration parameters are selected as $\zeta = \{0.1, 0.4, 0.7, 1\}$ and $\xi = \{0.1, 0.4, 0.7, 1\}$. The CNT volume fraction is varied according to $V_{\mathrm{CNT}} = \{0, 0.5, 1\,\%\}$. By combining all material schemes, distribution patterns and governing parameters, a comprehensive database containing 103 680 analytical samples was generated. This database was randomly partitioned into a training set (70 %), a validation set (15 %) and an independent test set (15 %), with stratification according to the Hardcore and Softcore schemes. Training of the Random Forest model required more than 10 s, while the prediction of a single natural frequency takes less than 1 ms, corresponding to a speed-up of roughly 500–1000 times relative to the analytical Galerkin evaluation of one sample. In addition to the complete database, independent datasets containing 10 368 analytical samples were extracted for each material scheme to perform a more detailed evaluation of the RF prediction accuracy for individual FG configurations.

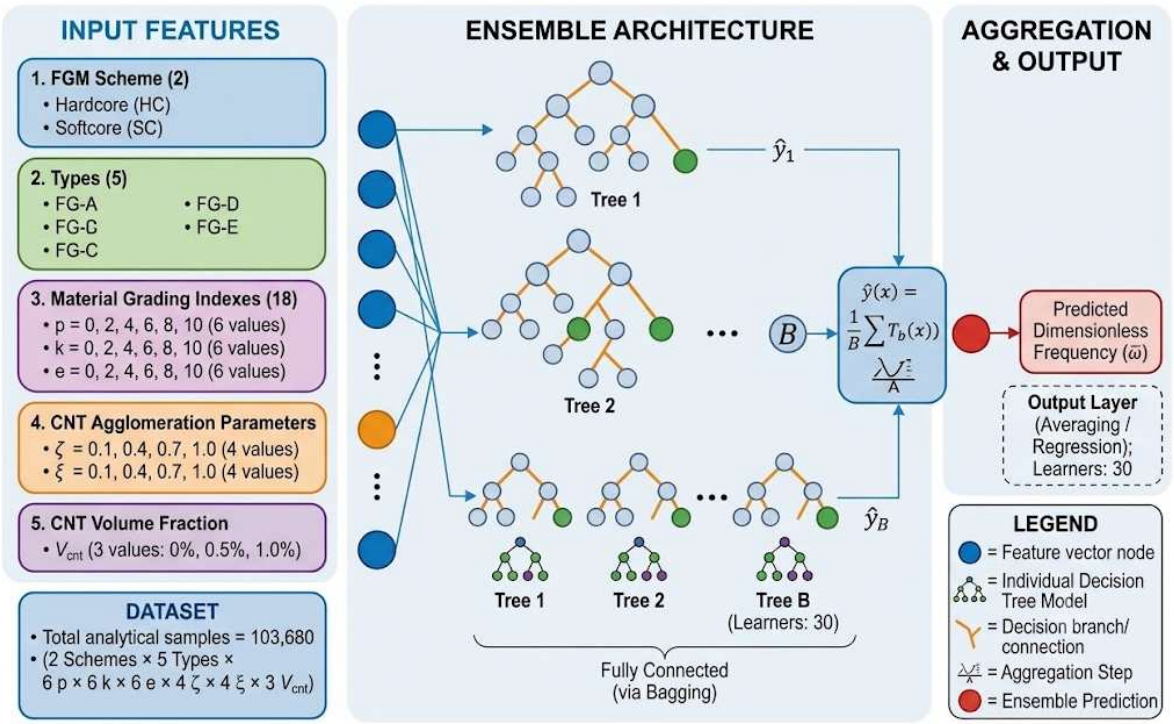


Fig. 15. Schematic representation of the Random Forest regression model for predicting the dimensionless natural frequency of coated FG-CNT cylindrical nanoshells.

7.2. Random Forest Regression

Random Forest regression constructs an ensemble of independent regression trees using bootstrap samples randomly selected from the original training dataset. At each node, only a random subset of predictor variables is considered for splitting, which reduces correlation among trees and significantly improves prediction robustness.

For a training dataset:

$$\mathcal{D} = \{(x_i, y_i)\}_{i=1}^{N} \tag{56}$$

where $x_i = [p, k, e, \zeta, \xi, V_{CNT}, Scheme, Type]$ represents the input variables and:

$$y_i = \bar{\omega} \tag{57}$$

denotes the normalized natural frequency, the prediction of the b^{th}regression tree is expressed as $T_b(x)$. The final Random Forest prediction is obtained by averaging the predictions of all trees:

$$\hat{y}(x) = \frac{1}{B}\sum_{b=1}^{B} T_b\,(x) \tag{58}$$

where B denotes the total number of regression trees. Each regression tree is generated by minimizing the mean squared prediction error:

$$\min \sum N\,(y_i - T_b(x_i))^2 \tag{59}$$

The combination of bootstrap aggregation and random feature selection enables the RF model to efficiently learn highly nonlinear relationships while preventing overfitting and improving prediction stability.

7.3. Model performance evaluation

The predictive performance of the proposed Random Forest (RF) model was evaluated using several complementary statistical indicators that quantify both the prediction accuracy and the computational efficiency. The Root Mean Square Error (RMSE) measures the standard deviation of the prediction errors and is expressed as:

$$RMSE = \sqrt{\frac{1}{N}\sum_{i=1}^{N}(y_i - \hat{y}_i)^2} \tag{60}$$

where $y_i$and $\hat{y}_i$denote the analytical and predicted normalized frequencies, respectively. The Mean Absolute Error (MAE), which represents the average absolute prediction error, is defined by:

$$MAE = \frac{1}{N}\sum_{i=1}^{N}|y_i - \hat{y}_i| \tag{61}$$

The Mean Squared Error (MSE), commonly used as the optimization criterion during model training, is given by:

$$MSE = \frac{1}{N}\sum_{i=1}^{N}(y_i - \hat{y}_i)^2 \tag{62}$$

To evaluate the relative prediction error independently of the response magnitude, the Mean Absolute Percentage Error (MAPE) is calculated as:

$$MAPE = \frac{100}{N}\sum_{i=1}^{N}\left|\frac{y_i - \hat{y}_i}{y_i}\right| \tag{63}$$

Besides these accuracy metrics, the computational efficiency of the RF model is assessed through the training time, corresponding to the total time required for model construction, and the prediction speed, defined as the number of observations processed per second during inference. These two indicators are particularly important for large-scale optimization and real-time prediction because they quantify the practical applicability of the proposed surrogate model.

7.4. Prediction results and discussion

Figure 16 presents the normalized performance profile of the Random Forest model for the complete analytical database containing 103,680 samples, including both Hardcore and Softcore coated FG-CNT nanoshells. The figure simultaneously summarizes the prediction accuracy and computational efficiency through the RMSE, MAE, MSE, MAPE, training time, and prediction speed. The consistently low prediction errors together with the small percentage errors indicate that the RF model accurately reproduces the vibration response over the entire design space. Furthermore, the short training time and high prediction speed demonstrate that the surrogate model can rapidly estimate the normalized frequencies without repeatedly solving the analytical governing equations. These results confirm that Random Forest provides an excellent compromise between prediction accuracy and computational efficiency, making it highly suitable for large-scale parametric analyses and optimization studies.

Figure 17 compares the predicted frequencies with the analytical solutions for the complete Hardcore and Softcore datasets. In both cases, the predicted values are tightly clustered around the 45° identity line, confirming an excellent agreement between the analytical formulation and the RF predictions. Quantitatively, the model achieves RMSE values of 0.027889 for the Hardcore shells and 0.034850 for the Softcore shells. The slightly lower prediction error obtained for the Hardcore configuration indicates that its vibration response exhibits a marginally more regular nonlinear behavior. In contrast, the wider variation of material properties in the Softcore shells—specifically the pronounced stiffness mismatch between the compliant core and the stiffer face sheets—induces highly non-linear transverse shear deformations and complex localized gradients across the thickness. Because the RF algorithm relies on axis-aligned decision splits that produce piecewise constant approximations, it faces a slightly more complex regression problem when mapping these sharp, continuous physical variations, leading to a visibly larger scatter. Nevertheless, both RMSE values remain extremely small, demonstrating the excellent overall generalization capability of the RF model. To further minimize prediction scatter for complex Softcore behaviors in future iterations, continuous surrogate models—such as Artificial Neural Networks (ANN) or Gaussian Process Regression (GPR)—could be employed, as their continuous kernels and activation functions are inherently better suited for resolving steep functional mechanical gradients.

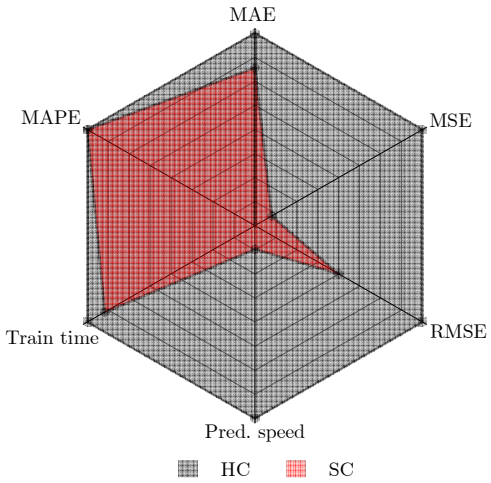


Fig. 16. Normalized performance profile of random forest predictions for hardcore vs. softcore shells.

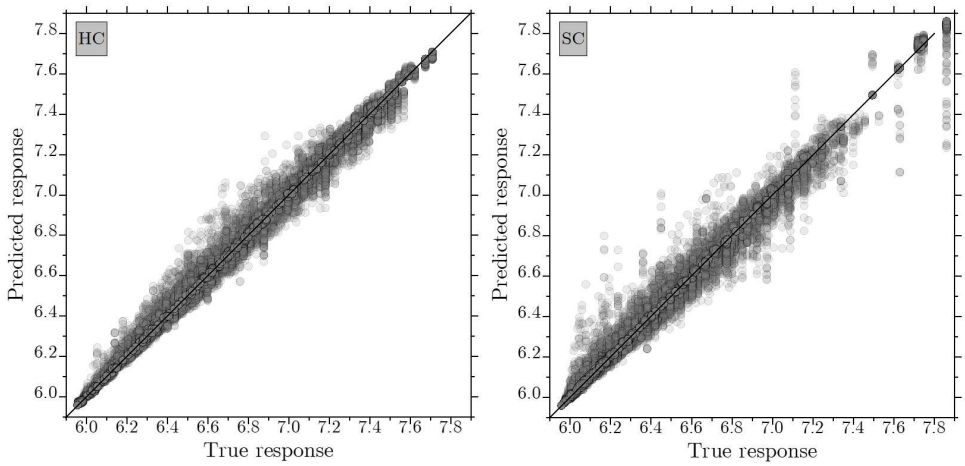


Fig. 17. Validation predicted vs. actual plot for predictions.

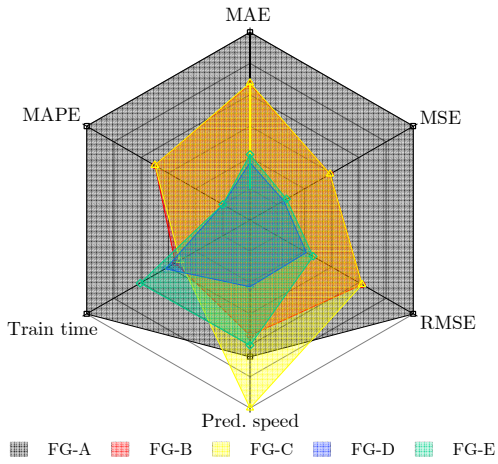


Fig. 18. Normalized performance profile of random forest predictions for hardcore FG shells patterns.

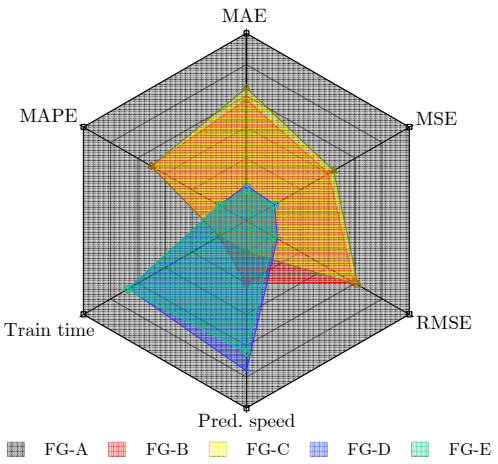


Fig. 19. Normalized performance profile of random forest predictions for softcore FG shells patterns.

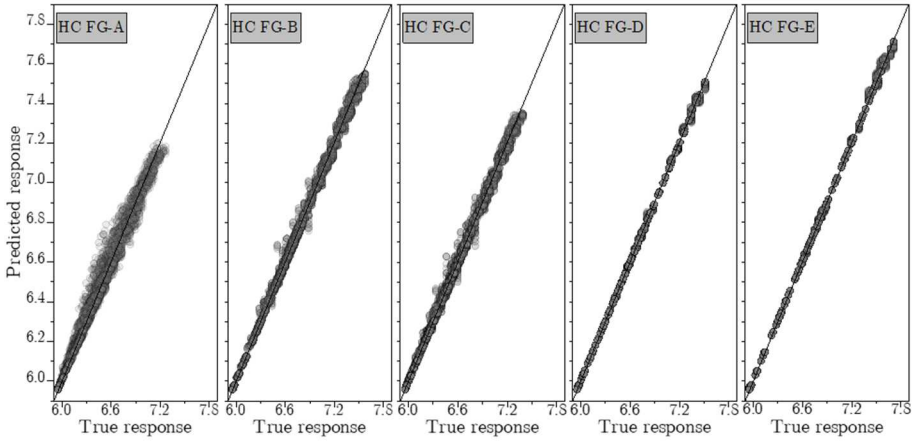


Fig. 20. Validation predicted vs actual plot for predictions for Hardcore FG shells.

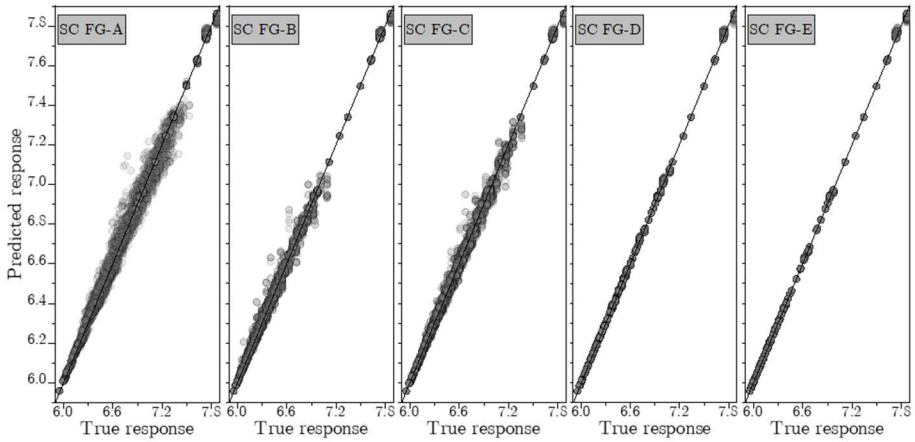


Fig. 21. Validation predicted vs. actual plot for predictions for Softcore FG shells.

Figure 18 illustrates the normalized performance profile of the Random Forest model for the Hardcore shell configurations using 10,368 analytical samples. The performance indicators reveal consistently small RMSE, MAE, MSE, and MAPE values for all FG distribution patterns, confirming the excellent predictive capability of the RF algorithm. In addition to its high accuracy, the RF model requires only a short training time while maintaining a high prediction speed, allowing rapid estimation of vibration frequencies for new design configurations. The combination of low prediction errors and efficient computation demonstrates that the RF model successfully captures the nonlinear influence of the grading indices, CNT agglomeration parameters, and reinforcement volume fraction in Hardcore shells.

Figure 19 presents the corresponding performance profile for the Softcore shell configurations. Similar to the Hardcore model, the Random Forest algorithm achieves very small RMSE, MAE, MSE, and MAPE values across all FG distribution patterns, indicating excellent agreement with the analytical solutions. Although the Softcore material distributions exhibit a slightly more complex parameter-to-frequency relationship, the computational performance remains highly satisfactory, as evidenced by the short training time and rapid prediction speed. These results demonstrate that the RF model preserves both accuracy and computational efficiency irrespective of the material distribution strategy, confirming its robustness over the complete parameter space.

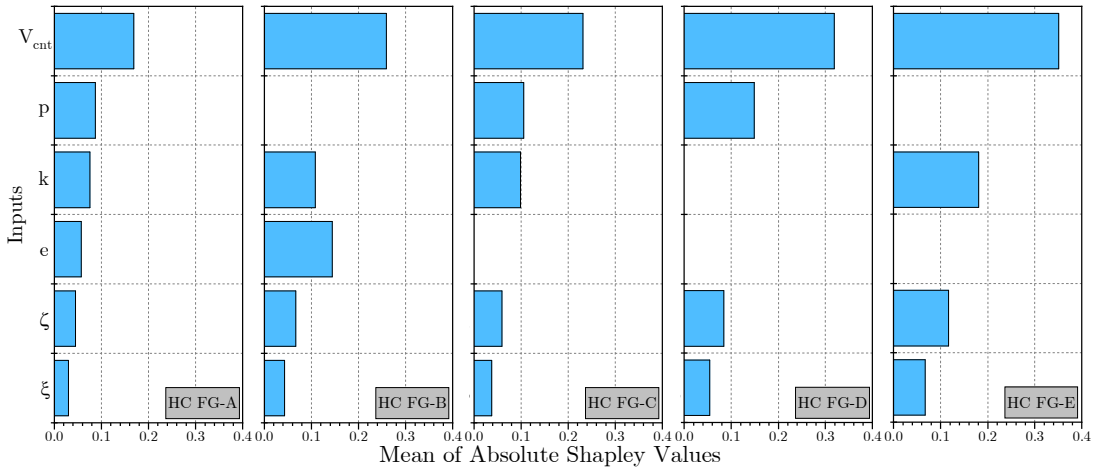


Fig. 22. Shapley material properties importance for Hardcore FG shells.

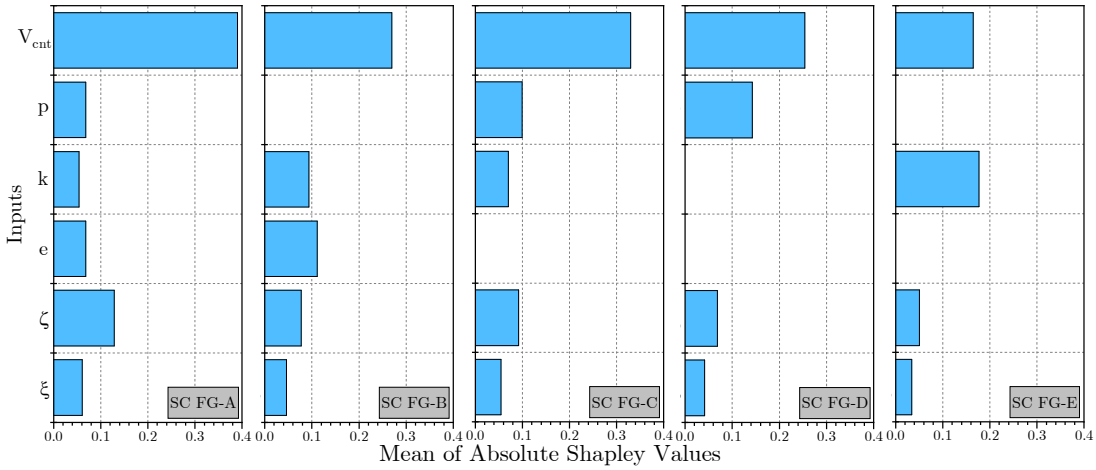


Fig. 23. Shapley material properties importance for Softcore FG shells.

The corresponding validation plots are presented in Figs. 20 and 21. For the Hardcore shells (Fig. 20), the predicted frequencies exhibit excellent agreement with the analytical solutions over the complete frequency range. Similar behavior is observed for the Softcore shells (Fig. 21), where almost all prediction points coincide with the identity line, confirming the robustness of the RF model.

The quantitative prediction errors further demonstrate the high accuracy of the proposed surrogate model. For the Hardcore shell configurations, the obtained RMSE values are 0.027573, 0.017199, 0.017179, 0.005921, and 0.007256 for the FG-A, FG-B, FG-C, FG-D, and FG-E distributions, respectively. The lowest prediction error is obtained for the FG-D configuration, closely followed by FG-E, whereas the tridirectional FG-A distribution produces the largest RMSE owing to its more complex nonlinear interaction among the material parameters.

Similarly, the Softcore shell configurations achieve RMSE values of 0.029705, 0.019202, 0.020023, 0.004812, and 0.004119 for the FG-A, FG-B, FG-C, FG-D, and FG-E distributions, respectively. Once again, FG-D and FG-E exhibit the smallest prediction errors, while FG-A remains the most challenging configuration because of its tridirectional functional gradation. Despite these differences, all RMSE values remain well below 0.03, confirming the remarkable prediction accuracy of the RF model for every investigated shell configuration.

Figures 22 and 23 present the SHAP (Shapley Additive Explanations) feature importance obtained from the Random Forest model for the Hardcore and Softcore shells, respectively. SHAP analysis provides a physically interpretable measure of the contribution of each design variable to the predicted vibration frequency. For both material schemes, the CNT volume fraction is identified as the dominant factor governing the vibration response, followed by the material grading indices p, k, and e, which directly control the spatial stiffness distribution throughout the shell thickness. The agglomeration parameters $\zeta$and ξexhibit comparatively smaller contributions but remain essential for describing the degradation of the effective mechanical properties caused by CNT clustering. The close agreement between the SHAP analysis and the analytical parametric study confirms that the RF model not only provides highly accurate predictions but also preserves the underlying physical behavior of coated FG-CNT nanoshells.

8. Conclusion

In this study, a novel analytical and data-driven framework was developed to investigate the free vibration response of coated FG-CNT nanoshells resting on a Winkler-Pasternak foundation. The primary novelty of this work lies in the unified integration of multi-directional material gradation (Hardcore and Softcore schemes with five distinct distribution patterns), dual-parameter CNT agglomeration, and nonlocal strain-gradient (NSGT) size effects. An exact analytical solution based on the higher-order shear deformation theory (HSDT) and the Galerkin approach was derived. From this mathematical framework, an unprecedented database of 103,680 samples was generated to train a Random Forest (RF) machine learning surrogate model for rapid, real-time frequency prediction.

The comprehensive parametric analysis and the predictive modeling yielded the following key findings:

- Increasing the inhomogeneity indexes enhances the rigidity of Hardcore FG-CNT shells, resulting in higher frequencies, but softens the Softcore configurations.
- Increasing the aspect ratio and the radius of curvature leads to a decrease in the dimensionless frequencies, regardless of the specific structural scheme utilized.
- The incorporation of CNT agglomeration significantly degrades the effective stiffness of the nanoshell, directly resulting in lower vibration frequencies.
- The inclusion of Winkler-Pasternak elastic foundations enhances the overall rigidity of the shells; increasing these foundation parameters proportionally increases the dimensionless frequency.
- The proposed RF surrogate model demonstrated exceptional predictive accuracy (RMSE < 0.035) and computational speed (under 1 millisecond per prediction), while SHAP analysis physically identified the CNT volume fraction and material grading indices as the dominant parameters governing the vibration response.

A primary limitation of this study is that the analytical approach is restricted to simple continuous structures with uniform thickness, such as beams, plates, and shells. Because the current framework cannot accommodate structural cutouts or complex shapes without numerical discretization, future work will extend this approach by utilizing the Finite Element Method (FEM) to generate training datasets for complex geometries like holed plates and shells. Additional critical next steps include investigating nonlinear transient dynamics under thermo-mechanical environments and exploring deep learning for real-time structural health monitoring.

Author Contributions

M.S. Abd-Elwahed contributed to the project administration, funding acquisition, data curation, resources, software, validation, formal analysis, investigation, original draft; A.A. Daikh contributed to the software, validation, conceptualization, methodology, formal analysis, investigation, original draft; A.S. Hamdi contributed to the conceptualization, formal analysis, investigation, resources, review and editing; R. Gamal contributed to the software, visualization, data curation, formal analysis, investigation, original draft; M.A. Eltaher contributed to the conceptualization, methodology, formal analysis, review and editing. All authors have read and agreed to the published version of the manuscript.

Acknowledgments

The authors acknowledge with thanks DSR for technical and financial support.

Conflict of Interest

The authors declared no potential conflicts of interest concerning the research, authorship, and publication of this article.

Funding

This project was funded by the Deanship of Scientific Research (DSR) at King Abdulaziz University, Jeddah, Saudi Arabia, under Grant No. (IPP 461-135-2025).

Data Availability Statements

The datasets generated and/or analyzed during the current study are available from the corresponding author on reasonable request.

References

[1] Milic, P., Marinkovic, D., Cojbašic, Ž., Geometrically nonlinear analysis of piezoelectric active laminated shells by means of isogeometric FE formulation, *Facta Universitatis, Series: Mechanical Engineering*, 23, 2025, 387.
[2] Fan, Y.H., She, G.L., Eltaher, M.A., Nonlinear vibrations of two-directional functionally graded spinning annular plates with variable thickness, *Thin-Walled Structures*, 2025, 113627.
[3] Daikh, A.A., Eltaher, M.A., Static analysis of tri-coated functionally graded nanoshells by Galerkin approach, *Computers and Concrete*, 36, 2025, 17.
[4] Nešic, N., Cajic, M., Karlicic, D., Lazarevic, M., Adhikari, S., Vibration and stability of a nonlinear nonlocal strain-gradient FG beam on a visco-Pasternak foundation, *Facta Universitatis, Series: Mechanical Engineering*, 23, 2025, 709.
[5] Alimoradzadeh, M., Tornabene, F., Panella, F., Dimitri, R., Theoretical study of the nonlinear dynamics of carbon-nanotube-reinforced composite beams under a moving mass, *Archive of Applied Mechanics*, 96, 2026, 44.
[6] Shi, D.L., Feng, X.Q., Huang, Y.Y., Hwang, K.C., Gao, H., The effect of nanotube waviness and agglomeration on the elastic property of carbon nanotube-reinforced composites, *Journal of Engineering Materials and Technology*, 126, 2004, 250-257.
[7] Hedayati, H., Aragh, B.S., Influence of graded agglomerated CNTs on vibration of CNT-reinforced annular sectorial plates resting on Pasternak foundation, *Applied Mathematics and Computation*, 218, 2012, 8715-8735.
[8] Aragh, B.S., Farahani, E.B., Barati, A.N., Natural frequency analysis of continuously graded carbon nanotube-reinforced cylindrical shells based on third-order shear deformation theory, *Mathematics and Mechanics of Solids*, 18, 2013, 264-284.
[9] Heshmati, M., Yas, M.H., Free vibration analysis of functionally graded CNT-reinforced nanocomposite beam using Eshelby-Mori-Tanaka approach, *Journal of Mechanical Science and Technology*, 27, 2013, 3403-3408.
[10] Kamarian, S., Salim, M., Dimitri, R., Tornabene, F., Free vibration analysis of conical shells reinforced with agglomerated carbon nanotubes, *International Journal of Mechanical Sciences*, 108, 2016, 157-165.
[11] Kamarian, S., Shakeri, M., Yas, M.H., Bodaghi, M., Pourasghar, A., Free vibration analysis of functionally graded nanocomposite sandwich beams resting on Pasternak foundation by considering the agglomeration effect of CNTs, *Journal of Sandwich Structures & Materials*, 17, 2015, 632-665.
[12] Tornabene, F., Fantuzzi, N., Bacciocchi, M., Linear static response of nanocomposite plates and shells reinforced by agglomerated carbon nanotubes, *Composites Part B: Engineering*, 115, 2017, 449-476.
[13] Tornabene, F., Fantuzzi, N., Bacciocchi, M., Viola, E., Effect of agglomeration on the natural frequencies of functionally graded carbon nanotube-reinforced laminated composite doubly-curved shells, *Composites Part B: Engineering*, 89, 2016, 187-218.
[14] Shokrieh, M.M., Rafiee, R., On the tensile behavior of an embedded carbon nanotube in polymer matrix with non-bonded interphase region, *Composite Structures*, 92, 2010, 647-652.



[15] He, X.Q., Eisenberger, M., Liew, K.M., The effect of van der Waals interaction modeling on the vibration characteristics of multiwalled carbon nanotubes, *Journal of Applied Physics*, 100, 2006, 124317.
[16] Strozzi, M., Pellicano, F., Linear vibrations of triple-walled carbon nanotubes, *Mathematics and Mechanics of Solids*, 23, 2018, 1456-1481.
[17] Barai, P., Weng, G.J., A theory of plasticity for carbon nanotube reinforced composites, *International Journal of Plasticity*, 27, 2011, 539-559.
[18] Yusufoglu, E., Avey, M., Nonlinear dynamic behavior of hyperbolic paraboloidal shells reinforced by carbon nanotubes with various distributions, *Journal of Applied and Computational Mechanics*, 7, 2021, 913-921.
[19] Nejati, M., Asanjarani, A., Dimitri, R., Tornabene, F., Static and free vibration analysis of functionally graded conical shells reinforced by carbon nanotubes, *International Journal of Mechanical Sciences*, 130, 2017, 383-398.
[20] Bisheh, H., Rabczuk, T., Wu, N., Effects of nanotube agglomeration on wave dynamics of carbon nanotube-reinforced piezocomposite cylindrical shells, *Composites Part B: Engineering*, 187, 2020, 107739.
[21] Zhang, L.W., Lei, Z.X., Liew, K.M., Computation of vibration solution for functionally graded carbon nanotube-reinforced composite thick plates resting on elastic foundations using the element-free IMLS-Ritz method, *Applied Mathematics and Computation*, 256, 2015, 488-504.
[22] Ziaei Moghadam, H., Faghidian, S.A., Jamal-Omidi, M., Agglomeration effects of carbon nanotube on residual stresses in polymer nano composite using experimental and analytical method, *Materials Research Express*, 6, 2019, 035009.
[23] Tavakoli Maleki, A., Pourseifi, M., Zakeri, M., Effect of agglomeration of the nanotubes on the vibration frequency of the multi-scale hybrid nanocomposite conical shells: a GDQ-based study, *Waves in Random and Complex Media*, 32, 2022, 359-380.
[24] Ajri, M., The nonlinear post-buckling behavior of FG cylindrical copper shell reinforced with carbon nanotubes with a polymer core, *Archive of Applied Mechanics*, 95, 2025, 19.
[25] Ozalp, A.F., Esen, I., Improved thermal stability of doubly-curved sandwich nanoplate with symmetric functionally graded face layers and an auxetic core under different structural configurations, *Archive of Applied Mechanics*, 96, 2026, 61.
[26] Nguyen, V.L., Tran, M.T., Limkatanyu, S., Mohammad-Sedighi, H., Rungamornrat, J., Reddy's third-order shear deformation shell theory for free vibration analysis of rotating stiffened advanced nanocomposite toroidal shell segments in thermal environments, *Acta Mechanica*, 233, 2022, 4659-4684.
[27] Saidi, A., Abouelregal, A.E., Kamel, E.S., Sedighi, H.M., Dynamic thermoelastic characteristics of a solid cylinder with voids: Integrating higher-order time-derivatives and a spatio-temporal Klein–Gordon approach, *Journal of Vibration Engineering & Technologies*, 14, 2026, 402.
[28] Avci, O., Abdeljaber, O., Kiranyaz, S., Hussein, M., Gabbouj, M., Inman, D.J., A review of vibration-based damage detection in civil structures: From traditional methods to Machine Learning and Deep Learning applications, *Mechanical Systems and Signal Processing*, 147, 2021, 107077.
[29] Jakkamputi, L., Devaraj, S., Marikkannan, S., Gnanasekaran, S., Ramasamy, S., Rakkiyannan, J., Xu, Y., Experimental and computational vibration analysis for diagnosing the defects in high performance composite structures using machine learning approach, *Applied Sciences*, 12, 2022, 12100.
[30] Challagulla, S.P., Bhargav, N.C., Parimi, C., Evaluation of damping modification factors for floor response spectra via machine learning model, *Structures*, 39, 2022, 679-690.
[31] de Sousa, A.A.S.R., da Silva Coelho, J., Machado, M.R., Dutkiewicz, M., Multiclass supervised machine learning algorithms applied to damage and assessment using beam dynamic response, *Journal of Vibration Engineering & Technologies*, 11, 2023, 2709-2731.
[32] Yan, Z., Zheng, S., Yang, F., Tai, X., Chen, Z., A simplified approach to recognize vortex-induced vibration response using machine learning, *Structural Engineering International*, 34, 2024, 670-682.
[33] Lin, Y., Ibraheem, A.A., Machine learning method as a tool to estimate the vibrations of the concrete structures reinforced by advanced nanocomposites, *Mechanics of Advanced Materials and Structures*, 32, 2025, 777-793.
[34] Zheng, F., Lu, Y., Duan, R., Chen, X., Koochakianfard, O., Machine learning and numerical approaches for vibration behavior prediction of rotating nanobeams in complex environments, *Mechanics of Advanced Materials and Structures*, 32, 2025, 3706-3723.
[35] Thai, H.T., Vo, T.P., A nonlocal sinusoidal shear deformation beam theory with application to bending, buckling, and vibration of nanobeams, *International Journal of Engineering Science*, 54, 2012, 58-66.
[36] Garg, A., Chalak, H.D., Zenkour, A.M., Belarbi, M., Houari, M., A review of available theories and methodologies for the analysis of nano isotropic, nano functionally graded, and CNT reinforced nanocomposite structures, *Archives of Computational Methods in Engineering*, 29, 2021, 2237-2270.
[37] Lam, D.C.C., Yang, F., Chong, A.C.M., Wang, J., Tong, P., Experiments and theory in strain gradient elasticity, *Journal of the Mechanics and Physics of Solids*, 51(8), 2003, 1477-1508.
[38] Gurtin, M.E., Murdoch, A.I., A continuum theory of elastic material surfaces, *Archive for Rational Mechanics and Analysis*, 57, 1975, 291-323.
[39] Gurtin, M.E., Murdoch, A.I., Surface stress in solids, *International Journal of Solids and Structures*, 14, 1978, 431-440.
[40] Van Vinh, P., Coupled nonlocal–strain gradient effects on the dynamic stability of functionally graded nanoplates resting on elastic foundations, *Mechanics Research Communications*, 155, 2026, 104709.
[41] Van Vinh, P., Coupled size-dependent damping mechanisms in viscoelastic functionally graded nanoplates on generalized foundations, *Engineering Structures*, 365, 2026, 123229.
[42] Van Vinh, P., Modified nonlocal strain gradient framework and ANN surrogate for size-dependent buckling of functionally graded nanoplates on Pasternak foundations, *Archives of Civil and Mechanical Engineering*, 26, 2026, 145.
[43] Van Thom, D., Chinh, V.M., Van Minh, P., Vu, N.D.A., Mechanical responses of nanoplates resting on viscoelastic foundations in multi-physical environments, *European Journal of Mechanics - A/Solids*, 106, 2024, 105309.
[44] Cuong, D.T.M., Van Nam, L., Van Thom, D., Van Doan, D., Research on the vibration absorption ability of sandwich nanoshells subjected to random loading, *Thin-Walled Structures*, 220, 2025, 114348.
[45] Van Ke, T., Van Minh, P., Van Thom, D., Duc, N.D., Static and dynamic analysis of doubly-curved functionally graded porous nanoshells integrated with piezoelectric surface layers and flexoelectric effect, *Computers & Structures*, 312, 2025, 107737.
[46] Van Ke, T., Van Thom, D., Dung, N.T., Van Chinh, N., Van Minh, P., Galerkin-Vlasov approach for bending analysis of flexoelectric doubly-curved sandwich nanoshells with piezoelectric/FGP/piezoelectric layers using the nonlocal strain theory, *Acta Mechanica Sinica*, 41, 2024, 123543.
[47] Alnujaie, A., Daikh, A.A., Ghazwani, M.H., Assie, A.E., Eltaher, M.A., Static response of fully coated porous functionally graded nanoshells, *Advances in Nano Research*, 18, 2025, 117.
[48] Matsunaga, H., Free vibration and stability of functionally graded shallow shells according to a 2D higher-order deformation theory, *Composite Structures*, 84, 2008, 132-146.
[49] Eringen, A.C., Plane waves in nonlocal micropolar elasticity, *International Journal of Engineering Science*, 22, 1984, 1113-1121.
[50] Lim, C.W., Zhang, G., Reddy, J.N., A higher-order nonlocal elasticity and strain gradient theory and its applications in wave propagation, *Journal of the Mechanics and Physics of Solids*, 78, 2015, 298-313.
[51] Balizadeh, A.M., Yaghootian, A., Sedighi, H.M., Tailoring low-frequency wave mitigation in Bezier-based curved metamaterials with external masses, *Journal of the Brazilian Society of Mechanical Sciences and Engineering*, 48, 2026, 574.
[52] Khare, R.K., Kant, T., Garg, A.K., Free vibration of composite and sandwich laminates with a higher-order facet shell element, *Composite Structures*, 65, 2004, 405-418.
[53] Fadaee, M., Atashipour, S., Hosseini-Hashemi, S., Free vibration analysis of Lévy-type functionally graded spherical shell panel using a new exact closed-form solution, *International Journal of Mechanical Sciences*, 77, 2013, 227-238.
[54] Van Vinh, P., Tounsi, A., Free vibration analysis of functionally graded doubly curved nanoshells using nonlocal first-order shear deformation theory with variable nonlocal parameters, *Thin-Walled Structures*, 174, 2022, 109084.
[55] Jouneghani, F.Z., Dimitri, R., Bacciocchi, M., Tornabene, F., Free vibration analysis of functionally graded porous doubly-curved shells based on the first-order shear deformation theory, *Applied Sciences*, 7, 2017, 1252.
[56] Chorfi, S.M., Houmat, A., Non-linear free vibration of a functionally graded doubly-curved shallow shell of elliptical plan-form, *Composite Structures*, 92, 2010, 2573-2581.
[57] Alijani, F., Amabili, M., Karagiozis, K., Bakhtiari-Nejad, F., Nonlinear vibrations of functionally graded doubly curved shallow shells, *Journal of Sound and Vibration*, 330, 2011, 1432-1454.
[58] Trinh, M.C., Kim, S.E., A three variable refined shear deformation theory for porous functionally graded doubly curved shell analysis, *Aerospace Science and Technology*, 94, 2019, 105356.

Appendix A

Stiffness matrix elements are:

$$K_{11} = A_{11}\int_0^a\int_0^b \frac{\partial^3 X_m}{\partial x^3} Y_n \frac{\partial X_m}{\partial x} Y_n \,\mathrm{d}x\mathrm{d}y + A_{66}\int_0^a\int_0^b \frac{\partial X_m}{\partial x}\frac{\partial^2 Y_n}{\partial y^2}\frac{\partial X_m}{\partial x} Y_n \,\mathrm{d}x\mathrm{d}y - \boldsymbol{\lambda}\Bigg[(A_{11}+A_{66})\int_0^a\int_0^b \frac{\partial^3 X_m}{\partial x^3}\frac{\partial^2 Y_n}{\partial y^2}\frac{\partial X_m}{\partial x} Y_n \,\mathrm{d}x\mathrm{d}y + A_{11}\int_0^a\int_0^b \frac{\partial^5 X_m}{\partial x^5} Y_n \frac{\partial X_m}{\partial x} Y_n \,\mathrm{d}x\mathrm{d}y + A_{66}\int_0^a\int_0^b \frac{\partial X_m}{\partial x}\frac{\partial^4 Y_n}{\partial y^4}\frac{\partial X_m}{\partial x} Y_n \,\mathrm{d}x\mathrm{d}y\Bigg] \tag{A.1}$$

$$K_{12} = (A_{12}+A_{66})\left(\int_0^a\int_0^b \frac{\partial X_m}{\partial x}\frac{\partial^2 Y_n}{\partial y^2}\frac{\partial X_m}{\partial x} Y_n \,\mathrm{d}x\mathrm{d}y - \boldsymbol{\lambda}\left[\int_0^a\int_0^b \frac{\partial^3 X_m}{\partial x^3}\frac{\partial^2 Y_n}{\partial y^2}\frac{\partial X_m}{\partial x} Y_n \,\mathrm{d}x\mathrm{d}y + \int_0^a\int_0^b \frac{\partial X_m}{\partial x}\frac{\partial^4 Y_n}{\partial y^4}\frac{\partial X_m}{\partial x} Y_n \,\mathrm{d}x\mathrm{d}y\right]\right) \tag{A.2}$$

$$K_{13} = \left(\frac{A_{11}}{R_x}+\frac{A_{12}}{R_y}\right)\left(\int_0^a\int_0^b \frac{\partial X_m}{\partial x} Y_n \frac{\partial X_m}{\partial x} Y_n \,\mathrm{d}x\mathrm{d}y - \lambda\left[\int_0^a\int_0^b \frac{\partial^3 X_m}{\partial x^3} Y_n \frac{\partial X_m}{\partial x} Y_n \,\mathrm{d}x\mathrm{d}y + \int_0^a\int_0^b \frac{\partial X_m}{\partial x}\frac{\partial^2 Y_n}{\partial y^2}\frac{\partial X_m}{\partial x} Y_n \,\mathrm{d}x\mathrm{d}y\right]\right) - B_{11}\int_0^a\int_0^b \frac{\partial^3 X_m}{\partial x^3} Y_n \frac{\partial X_m}{\partial x} Y_n \,\mathrm{d}x\mathrm{d}y - (B_{12}+2B_{66})\int_0^a\int_0^b \frac{\partial X_m}{\partial x}\frac{\partial^2 Y_n}{\partial y^2}\frac{\partial X_m}{\partial x} Y_n \,\mathrm{d}x\mathrm{d}y - \boldsymbol{\lambda}\left[-(B_{12}+2B_{66}+B_{11})\int_0^a\int_0^b \frac{\partial^3 X_m}{\partial x^3}\frac{\partial^2 Y_n}{\partial y^2}\frac{\partial X_m}{\partial x} Y_n \,\mathrm{d}x\mathrm{d}y - B_{11}\int_0^a\int_0^b \frac{\partial^5 X_m}{\partial x^5} Y_n \frac{\partial X_m}{\partial x} Y_n \,\mathrm{d}x\mathrm{d}y\right] \tag{A.3}$$

$$K_{14} = B^s_{11}\int_0^a\int_0^b \frac{\partial^3 X_m}{\partial x^3} Y_n \frac{\partial X_m}{\partial x} Y_n \,\mathrm{d}x\mathrm{d}y + B^s_{66}\int_0^a\int_0^b \frac{\partial X_m}{\partial x}\frac{\partial^2 Y_n}{\partial y^2}\frac{\partial X_m}{\partial x} Y_n \,\mathrm{d}x\mathrm{d}y - \boldsymbol{\lambda}\Bigg[(B^s_{11}+B^s_{66})\int_0^a\int_0^b \frac{\partial^3 X_m}{\partial x^3}\frac{\partial^2 Y_n}{\partial y^2}\frac{\partial X_m}{\partial x} Y_n \,\mathrm{d}x\mathrm{d}y + B^s_{11}\int_0^a\int_0^b \frac{\partial^5 X_m}{\partial x^5} Y_n \frac{\partial X_m}{\partial x} Y_n \,\mathrm{d}x\mathrm{d}y + B^s_{66}\int_0^a\int_0^b \frac{\partial X_m}{\partial x}\frac{\partial^4 Y_n}{\partial y^4}\frac{\partial X_m}{\partial x} Y_n \,\mathrm{d}x\mathrm{d}y\Bigg] \tag{A.4}$$

$$K_{15} = (B^s_{12}+B^s_{66})\left(\int_0^a\int_0^b \frac{\partial X_m}{\partial x}\frac{\partial^2 Y_n}{\partial y^2}\frac{\partial X_m}{\partial x} Y_n \,\mathrm{d}x\mathrm{d}y - \boldsymbol{\lambda}\left[\int_0^a\int_0^b \frac{\partial^3 X_m}{\partial x^3}\frac{\partial^2 Y_n}{\partial y^2}\frac{\partial X_m}{\partial x} Y_n \,\mathrm{d}x\mathrm{d}y + \int_0^a\int_0^b \frac{\partial X_m}{\partial x}\frac{\partial^4 Y_n}{\partial y^4}\frac{\partial X_m}{\partial x} Y_n \,\mathrm{d}x\mathrm{d}y\right]\right) \tag{A.5}$$

$$K_{21} = (A_{12}+A_{66})\left(\int_0^a\int_0^b \frac{\partial^2 X_m}{\partial x^1}\frac{\partial Y_n}{\partial y} X_m \frac{\partial Y_n}{\partial y}\mathrm{d}x\mathrm{d}y - \boldsymbol{\lambda}\left[\int_0^a\int_0^b \frac{\partial^4 X_m}{\partial x^4}\frac{\partial Y_n}{\partial y} X_m \frac{\partial Y_n}{\partial y}\mathrm{d}x\mathrm{d}y + \int_0^a\int_0^b \frac{\partial^2 X_m}{\partial x^2}\frac{\partial^3 Y_n}{\partial y^3} X_m \frac{\partial Y_n}{\partial y}\mathrm{d}x\mathrm{d}y\right]\right) \tag{A.6}$$

$$K_{22} = A_{22}\int_0^a\int_0^b X_m \frac{\partial^3 Y_n}{\partial y^3} X_m \frac{\partial Y_n}{\partial y}\mathrm{d}x\mathrm{d}y + A_{66}\int_0^a\int_0^b\int_0^b \frac{\partial^2 X_m}{\partial x^2}\frac{\partial Y_n}{\partial y} X_m \frac{\partial Y_n}{\partial y}\mathrm{d}x\mathrm{d}y - \boldsymbol{\lambda}\Bigg[(A_{22}+A_{66})\int_0^a\int_0^b \frac{\partial^2 X_m}{\partial x^2}\frac{\partial^3 Y_n}{\partial y^3} X_m \frac{\partial Y_n}{\partial y}\mathrm{d}x\mathrm{d}y + A_{22}\int_0^a\int_0^b X_m \frac{\partial^5 Y_n}{\partial y^5} X_m \frac{\partial Y_n}{\partial y}\mathrm{d}x\mathrm{d}y + A_{66}\int_0^a \frac{\partial^4 X_m}{\partial x^4}\frac{\partial Y_n}{\partial y} X_m \frac{\partial Y_n}{\partial y}\mathrm{d}x\mathrm{d}y\Bigg] \tag{A.7}$$

$$K_{23} = \left(\frac{A_{12}}{R_x}+\frac{A_{22}}{R_y}\right)\left(\int_0^a\int_0^b X_m \frac{\partial Y_n}{\partial y} X_m \frac{\partial Y_n}{\partial y}\mathrm{d}x\mathrm{d}y - \lambda\left[\int_0^a\int_0^b \frac{\partial^2 X_m}{\partial x^2}\frac{\partial Y_n}{\partial y} X_m \frac{\partial Y_n}{\partial y}\mathrm{d}x\mathrm{d}y + \int_0^a\int_0^b X_m \frac{\partial^3 Y_n}{\partial y^3} X_m \frac{\partial Y_n}{\partial y}\mathrm{d}x\mathrm{d}y\right]\right) - B_{22}\int_0^a\int_0^b X_m \frac{\partial^3 Y_n}{\partial y^3} X_m \frac{\partial Y_n}{\partial x}\mathrm{d}x\mathrm{d}y - (B_{12}+2B_{66})\int_0^a\int_0^b \frac{\partial^2 X_m}{\partial x^2}\frac{\partial Y_n}{\partial x} X_m \frac{\partial Y_n}{\partial x}\mathrm{d}x\mathrm{d}y - \lambda\Bigg(-(B_{22}+B_{12}+2B_{66})\int_0^a\int_0^b \frac{\partial^2 X_m}{\partial x^2}\frac{\partial^3 Y_n}{\partial y^3} X_m \frac{\partial Y_n}{\partial x}\mathrm{d}x\mathrm{d}y - (B_{12}+2B_{66})\int_0^a\int_0^b \frac{\partial^4 X_m}{\partial x^4}\frac{\partial Y_n}{\partial x} X_m \frac{\partial Y_n}{\partial x}\mathrm{d}x\mathrm{d}y - B_{22}\int_0^a\int_0^b X_m \frac{\partial^5 Y_n}{\partial y^5} X_m \frac{\partial Y_n}{\partial x}\mathrm{d}x\mathrm{d}y\Bigg) \tag{A.8}$$

$$K_{24} = (B^s_{12}+B^s_{66})\left(\int_0^a\int_0^b \frac{\partial^2 X_m}{\partial x^2}\frac{\partial Y_n}{\partial y} X_m \frac{\partial Y_n}{\partial y}\mathrm{d}x\mathrm{d}y - \lambda\left[\int_0^a\int_0^b \frac{\partial^4 X_m}{\partial x^4}\frac{\partial Y_n}{\partial y} X_m \frac{\partial Y_n}{\partial y}\mathrm{d}x\mathrm{d}y + \int_0^a\int_0^b \frac{\partial^2 X_m}{\partial x^2}\frac{\partial^3 Y_n}{\partial y^3} X_m \frac{\partial Y_n}{\partial y}\mathrm{d}x\mathrm{d}y\right]\right) \tag{A.9}$$

$$K_{25} = B_{22}^{s}\int_0^a\int_0^b X_m\frac{\partial^3 Y_n}{\partial y^3}X_m\frac{\partial Y_n}{\partial y}\,\mathrm{d}x\mathrm{d}y + B_{66}^{s}\int_0^a\int_0^b\frac{\partial^2 X_m}{\partial x^2}\frac{\partial Y_n}{\partial y}X_m\frac{\partial Y_n}{\partial y}\,\mathrm{d}x\mathrm{d}y$$
$$-\lambda\left[(B_{22}^{s}+B_{66}^{s})\int_0^a\int_0^b\frac{\partial^2 X_m}{\partial x^2}\frac{\partial^3 Y_n}{\partial y^3}X_m\frac{\partial Y_n}{\partial y}\,\mathrm{d}x\mathrm{d}y + B_{66}^{s}\int_0^a\int_0^b\frac{\partial^4 X_m}{\partial x^4}\frac{\partial Y_n}{\partial y}X_m\frac{\partial Y_n}{\partial y}\,\mathrm{d}x\mathrm{d}y + B_{22}^{s}\int_0^a\int_0^b X_m\frac{\partial^5 Y_n}{\partial y^5}X_m\frac{\partial Y_n}{\partial y}\,\mathrm{d}x\mathrm{d}y\right] \tag{A.10}$$

$$K_{31} = -\left(\frac{A_{11}}{R_x}+\frac{A_{12}}{R_y}\right)\left(\int_0^a\int_0^b\frac{\partial^2 X_n}{\partial x^2}Y_nX_mY_n\,\mathrm{d}x\mathrm{d}y - \lambda\left[\int_0^a\int_0^b\frac{\partial^4 X_n}{\partial x^4}Y_nX_mY_n\,\mathrm{d}x\mathrm{d}y + \int_0^a\int_0^b\frac{\partial^2 X_n}{\partial x^2}\frac{\partial^2 Y_n}{\partial y^2}X_mY_n\,\mathrm{d}x\mathrm{d}y\right]\right)$$
$$+B_{11}\int_0^a\int_0^b\frac{\partial^4 X_n}{\partial x^4}Y_nX_mY_n\,\mathrm{d}x\mathrm{d}y + (B_{12}+2B_{66})\int_0^a\int_0^b\frac{\partial^2 X_m}{\partial x^2}\frac{\partial^2 Y_n}{\partial y^2}X_mY_n\,\mathrm{d}x\mathrm{d}y$$
$$-\lambda\left[B_{11}\int_0^a\int_0^b\frac{\partial^6 X_n}{\partial x^6}Y_nX_mY_n\,\mathrm{d}x\mathrm{d}y + (B_{11}+B_{12}+2B_{66})\int_0^a\int_0^b\frac{\partial^4 X_m}{\partial x^4}\frac{\partial^2 Y_n}{\partial y^2}X_mY_n\,\mathrm{d}x\mathrm{d}y\right. \tag{A.11}$$
$$\left.+(B_{12}+2B_{66})\int_0^a\int_0^b\frac{\partial^2 X_m}{\partial x^2}\frac{\partial^4 Y_n}{\partial y^4}X_mY_n\,\mathrm{d}x\mathrm{d}y\right]$$

$$K_{32} = -\left(\frac{A_{12}}{R_x}+\frac{A_{22}}{R_y}\right)\left(\int_0^a\int_0^b X_m\frac{\partial^2 Y_n}{\partial y^2}X_mY_n\,\mathrm{d}x\mathrm{d}y - \lambda\left[\int_0^a\int_0^b\frac{\partial^2 X_m}{\partial x^2}\frac{\partial^2 Y_n}{\partial y^2}X_mY_n\,\mathrm{d}x\mathrm{d}y + \int_0^a\int_0^b X_m\frac{\partial^4 Y_n}{\partial y^4}X_mY_n\,\mathrm{d}x\mathrm{d}y\right]\right)$$
$$+B_{22}\int_0^a\int_0^b X_m\frac{\partial^4 Y_n}{\partial y^4}X_mY_n\,\mathrm{d}x\mathrm{d}y + (B_{12}+2B_{66})\int_0^a\int_0^b\frac{\partial^2 X_m}{\partial x^2}\frac{\partial^2 Y_n}{\partial y^2}X_mY_n\,\mathrm{d}x\mathrm{d}y$$
$$-\lambda\left[(B_{22}+B_{12}+2B_{66})\int_0^a\int_0^b\frac{\partial^2 X_m}{\partial x^2}\frac{\partial^4 Y_n}{\partial y^4}X_mY_n\,\mathrm{d}x\mathrm{d}y + (B_{12}+2B_{66})\int_0^a\int_0^b\frac{\partial^4 X_m}{\partial x^4}\frac{\partial^2 Y_n}{\partial y^2}X_mY_n\,\mathrm{d}x\mathrm{d}y\right. \tag{A.12}$$
$$\left.+B_{22}\int_0^a\int_0^b X_m\frac{\partial^6 Y_n}{\partial y^6}X_mY_n\,\mathrm{d}x\mathrm{d}y\right]$$

$$K_{33} = 2\left(\frac{B_{11}}{R_x}+\frac{B_{12}}{R_y}\right)\left(\int_0^a\int_0^b\frac{\partial^2 X_n}{\partial x^2}Y_nX_mY_n\,\mathrm{d}x\mathrm{d}y - \lambda\left[\int_0^a\int_0^b\frac{\partial^4 X_m}{\partial x^4}Y_nX_mY_n\,\mathrm{d}x\mathrm{d}y + \int_0^a\int_0^b\frac{\partial^2 X_n}{\partial x^2}\frac{\partial^2 Y_n}{\partial y^2}X_mY_n\,\mathrm{d}x\mathrm{d}y\right]\right)$$
$$+2\left(\frac{B_{12}}{R_x}+\frac{B_{22}}{R_y}\right)\left(\int_0^a\int_0^b X_m\frac{\partial^2 Y_n}{\partial y^2}X_mY_n\,\mathrm{d}x\mathrm{d}y - \lambda\left[\int_0^a\int_0^b\frac{\partial^2 X_m}{\partial x^2}\frac{\partial^2 Y_n}{\partial y^2}X_mY_n\,\mathrm{d}x\mathrm{d}y + \int_0^a\int_0^b X_m\frac{\partial^4 Y_n}{\partial y^4}X_mY_n\,\mathrm{d}x\mathrm{d}y\right]\right)$$
$$-\left(\frac{A_{11}}{{R_x}^2}+2\frac{A_{12}}{R_xR_y}+\frac{A_{22}}{{R_y}^2}\right)\left(\int_0^a\int_0^b X_mY_nX_mY_n\,\mathrm{d}x\mathrm{d}y - \lambda\left[\int_0^a\int_0^b\frac{\partial^2 X_m}{\partial x^2}Y_nX_mY_n\,\mathrm{d}x\mathrm{d}y + \int_0^a\int_0^b X_m\frac{\partial^2 Y_n}{\partial y^2}X_mY_n\,\mathrm{d}x\mathrm{d}y\right]\right)$$
$$-D_{11}\int_0^a\int_0^b\frac{\partial^4 X_m}{\partial x^4}Y_nX_mY_n\,\mathrm{d}x\mathrm{d}y - D_{22}\int_0^a\int_0^b X_m\frac{\partial^4 Y_n}{\partial y^4}X_mY_n\,\mathrm{d}x\mathrm{d}y - 2(D_{12}+2D_{66})\int_0^a\int_0^b\frac{\partial^2 X_m}{\partial x^2}\frac{\partial^2 Y_n}{\partial y^2}X_mY_n\,\mathrm{d}x\mathrm{d}y$$
$$-\lambda\left[-D_{11}\int_0^a\int_0^b\frac{\partial^6 X_m}{\partial x^6}Y_nX_mY_n\,\mathrm{d}x\mathrm{d}y - D_{22}\int_0^a\int_0^b\frac{\partial^2 X_m}{\partial x^2}\frac{\partial^4 Y_n}{\partial y^4}X_mY_n\,\mathrm{d}x\mathrm{d}y - 2(D_{12}+2D_{66})\int_0^a\int_0^b\frac{\partial^4 X_m}{\partial x^4}\frac{\partial^2 Y_n}{\partial y^2}X_mY_n\,\mathrm{d}x\mathrm{d}y\right. \tag{A.13}$$
$$\left.-D_{11}\int_0^a\int_0^b\frac{\partial^4 X_m}{\partial x^4}\frac{\partial^2 Y_n}{\partial y^2}X_mY_n\,\mathrm{d}x\mathrm{d}y - D_{22}\int_0^a\int_0^b X_m\frac{\partial^6 Y_n}{\partial y^6}X_mY_n\,\mathrm{d}x\mathrm{d}y - 2(D_{12}+2D_{66})\int_0^a\int_0^b\frac{\partial^2 X_m}{\partial x^2}\frac{\partial^4 Y_n}{\partial y^4}X_mY_n\,\mathrm{d}x\mathrm{d}y\right]$$
$$-k_w\left(\int_0^a\int_0^b X_mY_nX_mY_n\,\mathrm{d}x\mathrm{d}y - \mu\left[\int_0^a\int_0^b\frac{\partial^2 X_m}{\partial x^2}Y_nX_mY_n\,\mathrm{d}x\mathrm{d}y + \int_0^a\int_0^b X_m\frac{\partial^2 Y_n}{\partial y^2}X_mY_n\,\mathrm{d}x\mathrm{d}y\right]\right)$$
$$+k_S\left(\int_0^a\int_0^b\frac{\partial^2 X_m}{\partial x^2}Y_nX_mY_n\,\mathrm{d}x\mathrm{d}y - \mu\left[\int_0^a\int_0^b\frac{\partial^4 X_m}{\partial x^4}Y_nX_mY_n\,\mathrm{d}x\mathrm{d}y + \int_0^a\int_0^b\frac{\partial^2 X_m}{\partial x^2}\frac{\partial^2 Y_n}{\partial y^2}X_mY_n\,\mathrm{d}x\mathrm{d}y\right]\right)$$
$$+k_S\left(\int_0^a\int_0^b X_m\frac{\partial^2 Y_n}{\partial y^2}X_mY_n\,\mathrm{d}x\mathrm{d}y - \mu\left[\int_0^a\int_0^b\frac{\partial^2 X_m}{\partial x^2}\frac{\partial^2 Y_n}{\partial y^2}X_mY_n\,\mathrm{d}x\mathrm{d}y + \int_0^a\int_0^b X_m\frac{\partial^4 Y_n}{\partial y^4}X_mY_n\,\mathrm{d}x\mathrm{d}y\right]\right)$$

$$K_{34} = -\left(\frac{B_{11}^{s}}{R_x}+\frac{B_{12}^{s}}{R_y}\right)\left(\int_0^a\int_0^b\frac{\partial^2 X_n}{\partial x^2}Y_nX_mY_n\,\mathrm{d}x\mathrm{d}y - \lambda\left[\int_0^a\int_0^b\frac{\partial^4 X_m}{\partial x^4}Y_nX_mY_n\,\mathrm{d}x\mathrm{d}y + \int_0^a\int_0^b\frac{\partial^2 X_n}{\partial x^2}\frac{\partial^2 Y_n}{\partial y^2}X_mY_n\,\mathrm{d}x\mathrm{d}y\right]\right)$$
$$+D_{11}^{s}\int_0^a\int_0^b\frac{\partial^4 X_m}{\partial x^4}Y_nX_mY_n\,\mathrm{d}x\mathrm{d}y + (D_{12}^{s}+2D_{66}^{s})\int_0^a\int_0^b\frac{\partial^2 X_m}{\partial x^2}\frac{\partial^2 Y_n}{\partial y^2}X_mY_n\,\mathrm{d}x\mathrm{d}y$$
$$-\lambda\left[D_{11}^{s}\int_0^a\int_0^b\frac{\partial^6 X_m}{\partial x^6}Y_nX_mY_n\,\mathrm{d}x\mathrm{d}y + (D_{11}^{s}+D_{12}^{s}+2D_{66}^{s})\int_0^a\int_0^b\frac{\partial^4 X_m}{\partial x^4}\frac{\partial^2 Y_n}{\partial y^2}X_mY_n\,\mathrm{d}x\mathrm{d}y\right. \tag{A.14}$$
$$\left.+(D_{12}^{s}+2D_{66}^{s})\int_0^a\int_0^b\frac{\partial^2 X_m}{\partial x^2}\frac{\partial^4 Y_n}{\partial y^4}X_mY_n\,\mathrm{d}x\mathrm{d}y\right]$$

$$K_{35} = -\left(\frac{B_{12}^s}{R_x}+\frac{B_{22}^s}{R_y}\right)\left(\int_0^a\int_0^b X_m\frac{\partial^2 Y_n}{\partial y^2}X_mY_n\,\mathrm{d}x\mathrm{d}y-\lambda\left[\int_0^a\int_0^b\frac{\partial^2 X_m}{\partial x^2}\frac{\partial^2 Y_n}{\partial y^2}X_mY_n\,\mathrm{d}x\mathrm{d}y+\int_0^a\int_0^b X_m\frac{\partial^4 Y_n}{\partial y^4}X_mY_n\,\mathrm{d}x\mathrm{d}y\right]\right)$$
$$+D_{22}^s\int_0^a\int_0^b X_m\frac{\partial^4 Y_n}{\partial y^4}X_mY_n\,\mathrm{d}x\mathrm{d}y+(D_{12}^s+2D_{66}^s)\int_0^a\int_0^b\frac{\partial^2 X_m}{\partial x^2}\frac{\partial^2 Y_n}{\partial y^2}X_mY_n\,\mathrm{d}x\mathrm{d}y$$
$$-\lambda\left[(D_{12}^s+2D_{66}^s)\int_0^a\int_0^b\frac{\partial^4 X_m}{\partial x^4}\frac{\partial^2 Y_n}{\partial y^2}X_mY_n\,\mathrm{d}x\mathrm{d}y+D_{22}^s\int_0^a\int_0^b X_m\frac{\partial^6 Y_n}{\partial y^6}X_mY_n\,\mathrm{d}x\mathrm{d}y\right.$$
$$\left.+(D_{22}^s+D_{12}^s+2D_{66}^s)\int_0^a\int_0^b\frac{\partial^2 X_m}{\partial x^2}\frac{\partial^4 Y_n}{\partial y^4}X_mY_n\,\mathrm{d}x\mathrm{d}y\right] \tag{A.15}$$

$$K_{41} = B_{11}^s\int_0^a\int_0^b\frac{\partial^3 X_m}{\partial x^3}Y_n\frac{\partial X_m}{\partial x}Y_n\,\mathrm{d}x\mathrm{d}y+B_{66}^s\int_0^a\int_0^b\frac{\partial X_m}{\partial x}\frac{\partial^2 Y_n}{\partial y^2}\frac{\partial X_m}{\partial x}Y_n\,\mathrm{d}x\mathrm{d}y$$
$$-\lambda\left[B_{11}^s\int_0^a\int_0^b\frac{\partial^5 X_m}{\partial x^5}Y_n\frac{\partial X_m}{\partial x}Y_n\,\mathrm{d}x\mathrm{d}y+(B_{11}^s+B_{66}^s)\int_0^a\int_0^b\frac{\partial^3 X_m}{\partial x^3}\frac{\partial^2 Y_n}{\partial y^2}\frac{\partial X_m}{\partial x}Y_n\,\mathrm{d}x\mathrm{d}y\right.$$
$$\left.+B_{66}^s\int_0^a\int_0^b\frac{\partial X_m}{\partial x}\frac{\partial^4 Y_n}{\partial y^4}\frac{\partial X_m}{\partial x}Y_n\,\mathrm{d}x\mathrm{d}y\right] \tag{A.16}$$

$$K_{42} = (B_{12}^s+B_{66}^s)\left(\int_0^a\int_0^b\frac{\partial X_m}{\partial x}\frac{\partial^2 Y_n}{\partial y^2}\frac{\partial X_m}{\partial x}Y_n\,\mathrm{d}x\mathrm{d}y-\lambda\left[\int_0^a\int_0^b\frac{\partial^3 X_m}{\partial x^3}\frac{\partial^2 Y_n}{\partial y^2}\frac{\partial X_m}{\partial x}Y_n\,\mathrm{d}x\mathrm{d}y+\int_0^a\int_0^b\frac{\partial X_m}{\partial x}\frac{\partial^4 Y_n}{\partial y^4}\frac{\partial X_m}{\partial x}Y_n\,\mathrm{d}x\mathrm{d}y\right]\right) \tag{A.17}$$

$$K_{43} = \left(\frac{B_{11}^s}{R_x}+\frac{B_{12}^s}{R_y}\right)\left(\int_0^a\int_0^b\frac{\partial X_m}{\partial x}Y_n\frac{\partial X_m}{\partial x}Y_n\,\mathrm{d}x\mathrm{d}y-\lambda\left[\int_0^a\int_0^b\frac{\partial^3 X_m}{\partial x^3}Y_n\frac{\partial X_m}{\partial x}Y_n\,\mathrm{d}x\mathrm{d}y+\int_0^a\int_0^b\frac{\partial X_m}{\partial x}\frac{\partial^2 Y_n}{\partial y^2}\frac{\partial X_m}{\partial x}Y_n\,\mathrm{d}x\mathrm{d}y\right]\right)$$
$$-D_{11}^s\int_0^a\int_0^b\frac{\partial^3 X_m}{\partial x^3}Y_n\frac{\partial X_m}{\partial x}Y_n\,\mathrm{d}x\mathrm{d}y-(D_{12}^s+2D_{66}^s)\int_0^a\int_0^b\frac{\partial X_m}{\partial x}\frac{\partial^2 Y_n}{\partial y^2}\frac{\partial X_m}{\partial x}Y_n\,\mathrm{d}x\mathrm{d}y$$
$$-\lambda\left[-(D_{11}^s+D_{12}^s+2D_{66}^s)\int_0^a\int_0^b\frac{\partial^3 X_m}{\partial x^3}\frac{\partial^2 Y_n}{\partial y^2}\frac{\partial X_m}{\partial x}Y_n\,\mathrm{d}x\mathrm{d}y-D_{11}^s\int_0^a\int_0^b\frac{\partial^5 X_m}{\partial x^5}Y_n\frac{\partial X_m}{\partial x}Y_n\,\mathrm{d}x\mathrm{d}y\right.$$
$$\left.-(D_{12}^s+2D_{66}^s)\int_0^a\int_0^b\frac{\partial X_m}{\partial x}\frac{\partial^4 Y_n}{\partial y^4}\frac{\partial X_m}{\partial x}Y_n\,\mathrm{d}x\mathrm{d}y\right] \tag{A.18}$$

$$K_{44} = F_{11}^s\int_0^a\int_0^b\frac{\partial^3 X_m}{\partial x^3}Y_n\frac{\partial X_m}{\partial x}Y_n\,\mathrm{d}x\mathrm{d}y+F_{66}^s\int_0^a\int_0^b\frac{\partial X_m}{\partial x}\frac{\partial^2 Y_n}{\partial y^2}\frac{\partial X_m}{\partial x}Y_n\,\mathrm{d}x\mathrm{d}y-A_{44}^s\int_0^a\int_0^b\frac{\partial X_m}{\partial x}Y_n\frac{\partial X_m}{\partial x}Y_n\,\mathrm{d}x\mathrm{d}y$$
$$-\lambda\left[F_{11}^s\int_0^a\int_0^b\frac{\partial^5 X_m}{\partial x^5}Y_n\frac{\partial X_m}{\partial x}Y_n\,\mathrm{d}x\mathrm{d}y+(F_{66}^s+F_{11}^s)\int_0^a\int_0^b\frac{\partial^3 X_m}{\partial x^3}\frac{\partial^2 Y_n}{\partial y^2}\frac{\partial X_m}{\partial x}Y_n\,\mathrm{d}x\mathrm{d}y\right.$$
$$\left.-A_{44}^s\int_0^a\int_0^b\frac{\partial^3 X_m}{\partial x^3}Y_n\frac{\partial X_m}{\partial x}Y_n\,\mathrm{d}x\mathrm{d}y+F_{66}^s\int_0^a\int_0^b\frac{\partial X_m}{\partial x}\frac{\partial^4 Y_n}{\partial y^4}\frac{\partial X_m}{\partial x}Y_n\,\mathrm{d}x\mathrm{d}y-A_{44}^s\int_0^a\int_0^b\frac{\partial X_m}{\partial x}\frac{\partial^2 Y_n}{\partial y^2}\frac{\partial X_m}{\partial x}Y_n\,\mathrm{d}x\mathrm{d}y\right] \tag{A.19}$$

$$K_{45} = (F_{12}^s+F_{66}^s)\left(\int_0^a\int_0^b\frac{\partial X_m}{\partial x}\frac{\partial^2 Y_n}{\partial y^2}\frac{\partial X_m}{\partial x}Y_n\,\mathrm{d}x\mathrm{d}y-\lambda\left[\int_0^a\int_0^b\frac{\partial^3 X_m}{\partial x^3}\frac{\partial^2 Y_n}{\partial y^2}\frac{\partial X_m}{\partial x}Y_n\,\mathrm{d}x\mathrm{d}y+\int_0^a\int_0^b\frac{\partial X_m}{\partial x}\frac{\partial^4 Y_n}{\partial y^4}\frac{\partial X_m}{\partial x}Y_n\,\mathrm{d}x\mathrm{d}y\right]\right) \tag{A.20}$$

$$K_{15} = (B_{12}^s+B_{66}^s)\int_0^a\int_0^b\frac{\partial^2 X_m}{\partial x^2}\frac{\partial Y_n}{\partial y}X_m\frac{\partial Y_n}{\partial y}\mathrm{d}x\mathrm{d}y-\lambda\left[\int_0^a\int_0^b\frac{\partial^4 X_m}{\partial x^4}\frac{\partial Y_n}{\partial y}X_m\frac{\partial Y_n}{\partial y}\mathrm{d}x\mathrm{d}y+\int_0^a\int_0^b\frac{\partial^2 X_m}{\partial x^2}\frac{\partial^3 Y_n}{\partial y^3}X_m\frac{\partial Y_n}{\partial y}\mathrm{d}x\mathrm{d}y\right] \tag{A.21}$$

$$K_{52} = B_{22}^s\int_0^a\int_0^b X_m\frac{\partial^3 Y_n}{\partial y^3}X_m\frac{\partial Y_n}{\partial y}\mathrm{d}x\mathrm{d}y+B_{66}^s\int_0^a\int_0^b\frac{\partial^2 X_m}{\partial x^2}\frac{\partial Y_n}{\partial y}X_m\frac{\partial Y_n}{\partial y}\mathrm{d}x\mathrm{d}y$$
$$-\lambda\left((B_{22}^s+B_{66}^s)\int_0^a\int_0^b\frac{\partial^2 X_m}{\partial x^2}\frac{\partial^3 Y_n}{\partial y^3}X_m\frac{\partial Y_n}{\partial y}\mathrm{d}x\mathrm{d}y+B_{66}^s\int_0^a\int_0^b\frac{\partial^4 X_m}{\partial x^4}\frac{\partial Y_n}{\partial y}X_m\frac{\partial Y_n}{\partial y}\mathrm{d}x\mathrm{d}y\right.$$
$$\left.+B_{22}^s\int_0^a\int_0^b X_m\frac{\partial^5 Y_n}{\partial y^5}X_m\frac{\partial Y_n}{\partial y}\mathrm{d}x\mathrm{d}y\right) \tag{A.22}$$

$$K_{53} = \left(\frac{B_{12}^s}{R_x}+\frac{B_{22}^s}{R_y}\right)\left(\int_0^a\int_0^b X_m\frac{\partial Y_n}{\partial y}X_m\frac{\partial Y_n}{\partial y}\mathrm{d}x\mathrm{d}y-\lambda\left[\int_0^a\int_0^b\frac{\partial^2 X_m}{\partial x^2}\frac{\partial Y_n}{\partial y}X_m\frac{\partial Y_n}{\partial y}\mathrm{d}x\mathrm{d}y+\int_0^a\int_0^b X_m\frac{\partial^3 Y_n}{\partial y^3}X_m\frac{\partial Y_n}{\partial y}\mathrm{d}x\mathrm{d}y\right]\right) \tag{A.23}$$

$$-D_{22}^s\int_0^a\int_0^b X_m\frac{\partial^3 Y_n}{\partial y^3}X_m\frac{\partial Y_n}{\partial y}\mathrm{d}x\mathrm{d}y-(D_{12}^s+2D_{66}^s)\int_0^a\int_0^b\frac{\partial^2 X_m}{\partial x^2}\frac{\partial Y_n}{\partial y}X_m\frac{\partial Y_n}{\partial y}\mathrm{d}x\mathrm{d}y$$
$$-\lambda\left[-(D_{12}^s+2D_{66}^s)\int_0^a\int_0^b\frac{\partial^4 X_m}{\partial x^4}\frac{\partial Y_n}{\partial y}X_m\frac{\partial Y_n}{\partial y}\mathrm{d}x\mathrm{d}y-D_{22}^s\int_0^a\int_0^b X_m\frac{\partial^5 Y_n}{\partial y^5}X_m\frac{\partial Y_n}{\partial y}\mathrm{d}x\mathrm{d}y\right.$$
$$\left.-(D_{22}^s+D_{12}^s+2D_{66}^s)\int_0^a\int_0^b\frac{\partial^2 X_m}{\partial x^2}\frac{\partial^3 Y_n}{\partial y^3}X_m\frac{\partial Y_n}{\partial y}\mathrm{d}x\mathrm{d}y\right]$$

$$K_{54}=(F_{12}^s+F_{66}^s)\left(\int_0^a\int_0^b\frac{\partial^2 X_m}{\partial x^2}\frac{\partial Y_n}{\partial y}X_m\frac{\partial Y_n}{\partial y}\mathrm{d}x\mathrm{d}y-\lambda\left[\int_0^a\int_0^b\frac{\partial^4 X_m}{\partial x^4}\frac{\partial Y_n}{\partial y}X_m\frac{\partial Y_n}{\partial y}\mathrm{d}x\mathrm{d}y+\int_0^a\int_0^b\frac{\partial^2 X_m}{\partial x^2}\frac{\partial^3 Y_n}{\partial y^3}X_m\frac{\partial Y_n}{\partial y}\mathrm{d}x\mathrm{d}y\right]\right) \tag{A.24}$$

$$K_{55}=F_{22}^s\int_0^a\int_0^b X_m\frac{\partial^3 Y_n}{\partial y^3}X_m\frac{\partial Y_n}{\partial y}\mathrm{d}x\mathrm{d}y+F_{66}^s\int_0^a\int_0^b\frac{\partial^2 X_m}{\partial x^2}\frac{\partial Y_n}{\partial y}X_m\frac{\partial Y_n}{\partial y}\mathrm{d}x\mathrm{d}y-A_{55}^s\int_0^a\int_0^b X_m\frac{\partial Y_n}{\partial y}X_m\frac{\partial Y_n}{\partial y}\mathrm{d}x\mathrm{d}y$$
$$-\lambda\left((F_{22}^s+F_{66}^s)\int_0^a\int_0^b\frac{\partial^2 X_m}{\partial x^2}\frac{\partial^3 Y_n}{\partial y^3}X_m\frac{\partial Y_n}{\partial y}\mathrm{d}x\mathrm{d}y+F_{66}^s\int_0^a\int_0^b\frac{\partial^4 X_m}{\partial x^4}\frac{\partial Y_n}{\partial y}X_m\frac{\partial Y_n}{\partial y}\mathrm{d}x\mathrm{d}y\right. \tag{A.25}$$
$$\left.-A_{55}^s\int_0^a\int_0^b\frac{\partial^2 X_m}{\partial x^2}\frac{\partial Y_n}{\partial y}X_m\frac{\partial Y_n}{\partial y}\mathrm{d}x\mathrm{d}y+F_{22}^s\int_0^a\int_0^b X_m\frac{\partial^5 Y_n}{\partial y^5}X_m\frac{\partial Y_n}{\partial y}\mathrm{d}x\mathrm{d}y-A_{44}^s\int_0^a\int_0^b X_m\frac{\partial^3 Y_n}{\partial y^3}X_m\frac{\partial Y_n}{\partial y}\mathrm{d}x\mathrm{d}y\right)$$

Mass matrix elements are:

$$M_{11}=\left(I_0+2\frac{I_1}{R_x}+\frac{I_3}{{R_y}^2}\right)\left(\int_0^a\int_0^b\frac{\partial X_m}{\partial x}Y_n\frac{\partial X_m}{\partial x}Y_n\,\mathrm{d}x\mathrm{d}y-\mu\left[\int_0^a\int_0^b\frac{\partial^3 X_m}{\partial x^3}Y_n\frac{\partial X_m}{\partial x}Y_n\,\mathrm{d}x\mathrm{d}y+\int_0^a\int_0^b\frac{\partial X_m}{\partial x}\frac{\partial^2 Y_n}{\partial y^2}{}_n\frac{\partial X_m}{\partial x}Y_n\,\mathrm{d}x\mathrm{d}y\right]\right) \tag{A.26}$$

$$M_{13}=-\left(I_1+\frac{I_2}{R_x}\right)\left(\int_0^a\int_0^b\frac{\partial X_m}{\partial x}Y_n\frac{\partial X_m}{\partial x}Y_n\,\mathrm{d}x\mathrm{d}y-\mu\left[\int_0^a\int_0^b\frac{\partial^3 X_m}{\partial x^3}Y_n\frac{\partial X_m}{\partial x}Y_n\,\mathrm{d}x\mathrm{d}y+\int_0^a\int_0^b\frac{\partial X_m}{\partial x}\frac{\partial^2 Y_n}{\partial y^2}{}_n\frac{\partial X_m}{\partial x}Y_n\,\mathrm{d}x\mathrm{d}y\right]\right) \tag{A.27}$$

$$M_{14}=\left(I_3+\frac{I_4}{R_x}\right)\left(\int_0^a\int_0^b\frac{\partial X_m}{\partial x}Y_n\frac{\partial X_m}{\partial x}Y_n\,\mathrm{d}x\mathrm{d}y-\mu\left[\int_0^a\int_0^b\frac{\partial^3 X_m}{\partial x^3}Y_n\frac{\partial X_m}{\partial x}Y_n\,\mathrm{d}x\mathrm{d}y+\int_0^a\int_0^b\frac{\partial X_m}{\partial x}\frac{\partial^2 Y_n}{\partial y^2}{}_n\frac{\partial X_m}{\partial x}Y_n\,\mathrm{d}x\mathrm{d}y\right]\right) \tag{A.28}$$

$$M_{22}=\left(I_0+2\frac{I_1}{R_y}+\frac{I_2}{{R_y}^2}\right)\left(\int_0^a\int_0^b X_m\frac{\partial Y_n}{\partial y}X_m\frac{\partial Y_n}{\partial y}\mathrm{d}x\mathrm{d}y-\mu\left[\int_0^a\int_0^b\frac{\partial^2 X_m}{\partial x^2}\frac{\partial Y_n}{\partial y}X_m\frac{\partial Y_n}{\partial y}\mathrm{d}x\mathrm{d}y+\int_0^a\int_0^b X_m\frac{\partial^3 Y_n}{\partial y^3}X_m\frac{\partial Y_n}{\partial y}\mathrm{d}x\mathrm{d}y\right]\right) \tag{A.29}$$

$$M_{23}=-\left(I_1+\frac{I_2}{R_y}\right)\left(\int_0^a\int_0^b X_m\frac{\partial Y_n}{\partial y}X_m\frac{\partial Y_n}{\partial y}\mathrm{d}x\mathrm{d}y-\mu\left[\int_0^a\int_0^b\frac{\partial^2 X_m}{\partial x^2}\frac{\partial Y_n}{\partial y}X_m\frac{\partial Y_n}{\partial y}\mathrm{d}x\mathrm{d}y+\int_0^a\int_0^b X_m\frac{\partial^3 Y_n}{\partial y^3}X_m\frac{\partial Y_n}{\partial y}\mathrm{d}x\mathrm{d}y\right]\right) \tag{A.30}$$

$$M_{25}=-\left(I_3+\frac{I_4}{R_y}\right)\int_0^a\int_0^b X_m\frac{\partial Y_n}{\partial y}X_m\frac{\partial Y_n}{\partial y}\mathrm{d}x\mathrm{d}y \tag{A.31}$$

$$M_{31}=\left(I_1+\frac{I_2}{R_x}\right)\left(\int_0^a\int_0^b\frac{\partial^2 X_m}{\partial x^2}Y_nX_mY_n\,\mathrm{d}x\mathrm{d}y-\mu\left[\int_0^a\int_0^b\frac{\partial^4 X_m}{\partial x^4}Y_nX_mY_n\,\mathrm{d}x\mathrm{d}y+\int_0^a\int_0^b\frac{\partial^2 X_m}{\partial x^2}\frac{\partial^2 Y_n}{\partial y^2}X_mY_n\,\mathrm{d}x\mathrm{d}y\right]\right) \tag{A.32}$$

$$M_{32}=\left(I_1+\frac{I_2}{R_y}\right)\left(\int_0^a\int_0^b X_m\frac{\partial^2 Y_n}{\partial y^2}X_mY_n\,\mathrm{d}x\mathrm{d}y-\mu\left[\int_0^a\int_0^b\frac{\partial^2 X_m}{\partial x^2}\frac{\partial^2 Y_n}{\partial y^2}X_mY_n\,\mathrm{d}x\mathrm{d}y+\int_0^a\int_0^b X_m\frac{\partial^4 Y_n}{\partial y^4}X_mY_n\,\mathrm{d}x\mathrm{d}y\right]\right) \tag{A.33}$$

$$M_{33}=I_0\left(\int_0^a\int_0^b X_mY_nX_mY_n\,\mathrm{d}x\mathrm{d}y-\mu\left[\int_0^a\int_0^b\frac{\partial^2 X_m}{\partial x^2}Y_nX_mY_n\,\mathrm{d}x\mathrm{d}y+\int_0^a\int_0^b X_m\frac{\partial^2 Y_n}{\partial y^2}X_mY_n\,\mathrm{d}x\mathrm{d}y\right]\right)$$
$$-I_2\left(\int_0^a\int_0^b\frac{\partial^2 X_m}{\partial x^2}Y_nX_mY_n\,\mathrm{d}x\mathrm{d}y-\mu\left[\int_0^a\int_0^b\frac{\partial^4 X_m}{\partial x^4}Y_nX_mY_n\,\mathrm{d}x\mathrm{d}y+2\int_0^a\int_0^b\frac{\partial^2 X_m}{\partial x^2}\frac{\partial^2 Y_n}{\partial y^2}X_mY_n\,\mathrm{d}x\mathrm{d}y\right]\right. \tag{A.34}$$
$$\left.+\int_0^a\int_0^b X_m\frac{\partial^2 Y_n}{\partial y^2}X_mY_n\,\mathrm{d}x\mathrm{d}y-\mu\int_0^a\int_0^b X_m\frac{\partial^4 Y_n}{\partial y^4}X_mY_n\,\mathrm{d}x\mathrm{d}y\right)$$

$$M_{34}=-I_4\left(\int_0^a\int_0^b\frac{\partial^2 X_m}{\partial x^2}Y_nX_mY_n\,\mathrm{d}x\mathrm{d}y-\mu\left[\int_0^a\int_0^b\frac{\partial^4 X_m}{\partial x^4}Y_nX_mY_n\,\mathrm{d}x\mathrm{d}y+\int_0^a\int_0^b\frac{\partial^2 X_m}{\partial x^2}\frac{\partial^2 Y_n}{\partial y^2}X_mY_n\,\mathrm{d}x\mathrm{d}y\right]\right) \tag{A.35}$$

$$M_{34} = -I_4 \left(\int_0^a \int_0^b X_m \frac{\partial^2 Y_n}{\partial y^2} X_m Y_n \, \mathrm{d}x\mathrm{d}y - \mu \left[\int_0^a \int_0^b \frac{\partial^2 X_m}{\partial x^2} \frac{\partial^2 Y_n}{\partial y^2} X_m Y_n \, \mathrm{d}x\mathrm{d}y + \int_0^a \int_0^b X_m \frac{\partial^4 Y_n}{\partial y^4} X_m Y_n \, \mathrm{d}x\mathrm{d}y \right] \right) \tag{A.36}$$

$$M_{41} = \left(I_3 + \frac{I_4}{R_x} \right) \left(\int_0^a \int_0^b \frac{\partial X_m}{\partial x} Y_n \frac{\partial X_m}{\partial x} Y_n \, \mathrm{d}x\mathrm{d}y - \mu \left[\int_0^a \int_0^b \frac{\partial^3 X_m}{\partial x^3} Y_n \frac{\partial X_m}{\partial x} Y_n \, \mathrm{d}x\mathrm{d}y + \int_0^a \int_0^b \frac{\partial X_m}{\partial x} \frac{\partial^2 Y_n}{\partial y^2} \frac{\partial X_m}{\partial x} Y_n \, \mathrm{d}x\mathrm{d}y \right] \right) \tag{A.37}$$

$$M_{43} = -I_4 \left(\int_0^a \int_0^b \frac{\partial X_m}{\partial x} Y_n \frac{\partial X_m}{\partial x} Y_n \, \mathrm{d}x\mathrm{d}y - \mu \left[\int_0^a \int_0^b \frac{\partial^3 X_m}{\partial x^3} Y_n \frac{\partial X_m}{\partial x} Y_n \, \mathrm{d}x\mathrm{d}y + \int_0^a \int_0^b \frac{\partial X_m}{\partial x} \frac{\partial^2 Y_n}{\partial y^2} \frac{\partial X_m}{\partial x} Y_n \, \mathrm{d}x\mathrm{d}y \right] \right) \tag{A.38}$$

$$M_{44} = I_5 \left(\int_0^a \int_0^b \frac{\partial X_m}{\partial x} Y_n \frac{\partial X_m}{\partial x} Y_n \, \mathrm{d}x\mathrm{d}y - \mu \left[\int_0^a \int_0^b \frac{\partial^3 X_m}{\partial x^3} Y_n \frac{\partial X_m}{\partial x} Y_n \, \mathrm{d}x\mathrm{d}y + \int_0^a \int_0^b \frac{\partial X_m}{\partial x} \frac{\partial^2 Y_n}{\partial y^2} \frac{\partial X_m}{\partial x} Y_n \, \mathrm{d}x\mathrm{d}y \right] \right) \tag{A.39}$$

$$M_{52} = \left(I_3 + \frac{I_4}{R_y} \right) \left(\int_0^a \int_0^b X_m \frac{\partial Y_n}{\partial y} X_m \frac{\partial Y_n}{\partial y} \mathrm{d}x\mathrm{d}y - \mu \left[\int_0^a \int_0^b \frac{\partial^2 X_m}{\partial x^2} \frac{\partial Y_n}{\partial y} X_m \frac{\partial Y_n}{\partial y} \mathrm{d}x\mathrm{d}y + \int_0^a \int_0^b X_m \frac{\partial^3 Y_n}{\partial y^3} X_m \frac{\partial Y_n}{\partial y} \mathrm{d}x\mathrm{d}y \right] \right) \tag{A.40}$$

$$M_{53} = -I_4 \left(\int_0^a \int_0^b X_m \frac{\partial Y_n}{\partial y} X_m \frac{\partial Y_n}{\partial y} \mathrm{d}x\mathrm{d}y - \mu \left[\int_0^a \int_0^b \frac{\partial^2 X_m}{\partial x^2} \frac{\partial Y_n}{\partial y} X_m \frac{\partial Y_n}{\partial y} \mathrm{d}x\mathrm{d}y + \int_0^a \int_0^b X_m \frac{\partial^3 Y_n}{\partial y^3} X_m \frac{\partial Y_n}{\partial y} \mathrm{d}x\mathrm{d}y \right] \right) \tag{A.41}$$

$$M_{12} = M_{15} = M_{21} = M_{24} = M_{42} = M_{45} = M_{51} = M_{54} = M_{55} = 0 \tag{A.42}$$

ORCID iD

Mohamed S. Abd-Elwahed https://orcid.org/0000-0003-1381-9325
Ahmed Amine Daikh http://orcid.org/0000-0002-4666-2750
Amin Sami Hamdi https://orcid.org/0000-0001-5003-5349
Rania Gamal https://orcid.org/0009-0001-6551-2280
Mohamed A. Eltaher https://orcid.org/0000-0003-3116-2101

© 2026 Shahid Chamran University of Ahvaz, Ahvaz, Iran. This article is an open access article distributed under the terms and conditions of the Creative Commons Attribution-NonCommercial 4.0 International (CC BY-NC 4.0 license) (http://creativecommons.org/licenses/by-nc/4.0/).

How to cite this article: Abd-Elwahed M.S., et al. Data-Driven and Analytical Investigation of Free Vibration in Agglomerated FG-CNT Coated Nanoshells, *J. Appl. Comput. Mech.*, xx(x), 2026, 1–26. https://doi.org/10.22055/jacm.2026.49723.6193

Publisher's Note Shahid Chamran University of Ahvaz remains neutral with regard to jurisdictional claims in published maps and institutional affiliations.